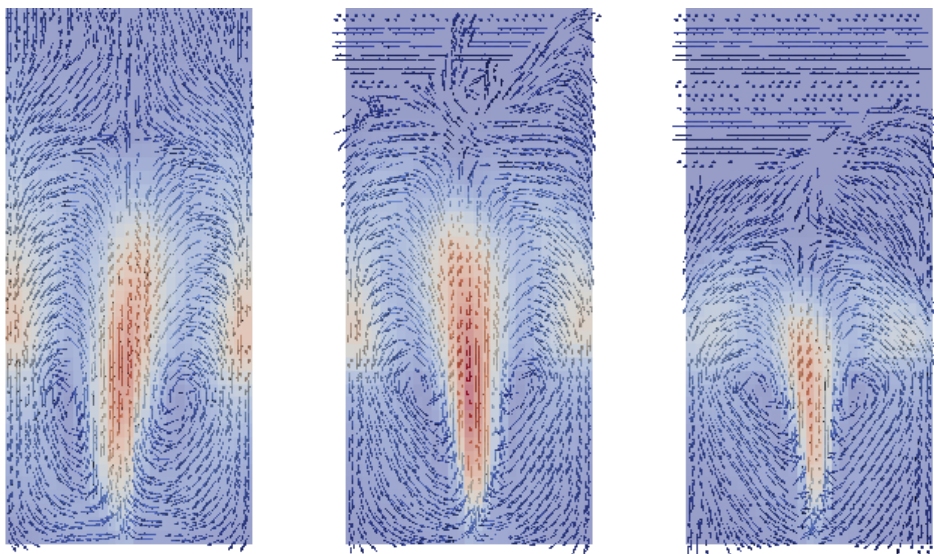




# CHALMERS

---



## Large scale simulation of particle coating using coupled CFD-DEM

Master's thesis in Applied Mechanics

ANAND HARIHARAN



MASTER'S THESIS IN APPLIED MECHANICS

Large scale simulation of particle coating using coupled CFD-DEM

ANAND HARIHARAN

Department of Mechanics and Maritime Sciences

Division of Fluid Dynamics

CHALMERS UNIVERSITY OF TECHNOLOGY

Göteborg, Sweden 2020

Large scale simulation of particle coating using coupled CFD-DEM  
ANAND HARIHARAN

© ANAND HARIHARAN, 2020

Master's thesis 2020:75  
Department of Mechanics and Maritime Sciences  
Division of Fluid Dynamics  
Chalmers University of Technology  
SE-412 96 Göteborg  
Sweden  
Telephone: +46 (0)31-772 1000

Chalmers Reproservice  
Göteborg, Sweden 2020

Large scale simulation of particle coating using coupled CFD-DEM  
Master's thesis in Applied Mechanics  
ANAND HARIHARAN  
Department of Mechanics and Maritime Sciences  
Division of Fluid Dynamics  
Chalmers University of Technology

## ABSTRACT

Spouted fluidized beds are widely used for particle coating because of its excellent mixing rates and favorable heat and mass transfer characteristics. The combination of Computational Fluid Dynamics (CFD) and the Discrete Element Method (DEM) has previously been employed for simulation of the complex phenomena of such processes. However, simulating a fluidized bed on a large scale with DEM requires exceptional computational power as all the interactions between the particles are fully resolved. In addition, simulating the spray droplets further increases the computational demand. Accordingly, coupled DEM and CFD simulations with a well resolved spray have typically been limited to system sizes from a few thousand up to much less than a million particles.

The goal of the current thesis was to perform spray coating simulations on systems with more than 1 million particles, including a Lagrangian spray phase and a well resolved fluid. The thesis is carried out using the DEM-CFD solver IPS Fluidization<sup>TM</sup> developed at Fraunhofer Chalmers Centre. The solver is based on an in-house DEM code and the in-house immersed boundary CFD code IBOFlow<sup>®</sup>. Due to heavy use of the Graphical Processing Unit (GPU), the code allows simulating a large number of particles and a well resolved fluid on a standard desktop computer.

In the first part of the thesis, single spout simulations are carried out to validate the coupled solver. The simulations show excellent agreement with the experimental data available in the open literature. Further, 1D studies are conducted for verifying the heat transfer model. The numerical predictions are shown to be accurate based on comparisons with analytical 1D models. Finally, large scale simulations including the spray and drying are conducted on a Wurster bed system with both the particles and the spray considered in a Lagrangian sense. The simulations show the versatility of the tool and the possibility to e.g. characterize the particle coating thickness in terms of the original particle size, as well as it proves applicability to cases with more than 1 million particles.

Keywords: CFD, DEM, particle coating, Wurster bed, fluidization, GPU

## ACKNOWLEDGEMENTS

I would like to express my immense gratitude for my supervisor and my mentor Klas Jareteg who guided me throughout my Master's program until my thesis. I am extremely grateful for the immense knowledge I had gained from him from the interesting discussions. Without his continuous guidance and persistent help my thesis would not have been possible.

I would like to extend my gratitude for Franziska Hunger for guiding me in conducting various simulations in my Master's thesis.

I would also like to thank Fredrik Edelvik (Head of department) at Fraunhofer-Chalmers Centre (FCC) for extending me an opportunity to work as a contracted student until my thesis at FCC. I would also like to thank FCC for providing me with required computational resources while pursuing my thesis.

I extend my gratitude for my examiner Srdjan Sasic for his valuable feedbacks and guidance during the course of this thesis.

Finally, I would like to thank my family and friends, who have been my constant source of motivation and support during my master's journey.

# Nomenclature

## Subscripts

$d$	Droplets
$f$	Fluid
$p$	Particle
$amb$	Ambient conditions
$cell$	Cell
$ref$	Reference conditions

## Abbreviations

CFD	Computational Fluid Dynamics
CPU	Central Processing Unit
DEM	Discrete Element Method
GPU	Graphics Processing Unit
PEPT	Positron emission particle tracking
PIV	Particle image velocimetry
TG	Transfer Grid

## Notation

$\beta$	Drag coefficient
$\mathbf{u}$	Fluid velocity
$\mathbf{v}$	Velocity of particle
$\delta_n$	Normal particle overlap
$\epsilon$	Volume fraction
$\eta_n$	Normal coefficient of viscous dissipation
$\mu$	Shear viscosity
$\omega$	Angular velocity
$\rho$	Density
$\tau$	Newtonian stress tensor
$\Delta H_{evap}$	Enthalpy of evaporation
$C_d$	Coefficient of drag
$C_p$	Heat capacity

$f_n$	Normal force
$h_f$	Heat transfer coefficient
$I_p$	Inertia
$k_m$	Mass transfer coefficient
$K_n$	Normal spring constant
$M$	Torque
$\dot{m}$	Mass flow rate
$Nu$	Nusselt number
$Q_a$	Heat flow per unit volume from particle to fluid
$Re$	Dimensionless Reynolds number
$S_m$	Source term for coupling mass transfer between particle and fluid
$S_p$	Body force exerted by particles on fluid
$Sc$	Schmidt number
$V_p$	Volume of particle
$w_f^*$	Saturated mass concentration of moisture in gas film layer around particle
$w_f$	Mass concentration of moisture in the bulk of the gas phase
$X_w$	Moisture content
$X_{d,s}$	Mole fraction of moisture at particle surface
A	Area
D	Diffusivity
d	Diameter
g	Gravitational acceleration constant
k	Thermal conductivity
m	Mass
p	Pressure
Pr	Prandtl number



# CONTENTS

<b>Abstract</b>	<b>i</b>
<b>Acknowledgements</b>	<b>ii</b>
<b>Contents</b>	<b>v</b>
<b>1 Introduction</b>	<b>2</b>
1.1 Physics of fluidized beds . . . . .	2
1.2 Physics of spouted fluidized beds . . . . .	2
1.3 Modeling of spouted fluidized beds . . . . .	3
1.4 Purpose of the project . . . . .	5
1.5 Simulation software . . . . .	5
1.6 Experimental Data . . . . .	6
1.7 Structure of the thesis . . . . .	7
<b>2 Theory</b>	<b>8</b>
2.1 Computational Fluid Dynamics . . . . .	8
2.1.1 Mass and momentum conservation . . . . .	8
2.1.2 Heat transfer . . . . .	9
2.1.3 Moisture conservation equation . . . . .	9
2.2 Discrete Element Method . . . . .	9
2.2.1 Particle Governing Equation . . . . .	10
2.2.2 Heat transfer Model . . . . .	12
2.2.3 Mass transfer model . . . . .	13
2.3 Spray droplets . . . . .	14
2.4 Multiphase Coupling . . . . .	14
2.4.1 Momentum Exchange . . . . .	15
2.4.2 Energy exchange between the phases . . . . .	17
2.4.3 Mass exchange between the phases . . . . .	18
<b>3 Methodology</b>	<b>19</b>
3.1 CFD solution procedure . . . . .	19
3.2 DEM algorithm . . . . .	19
3.3 Coupling method . . . . .	20
3.3.1 Data transfer . . . . .	21
3.3.2 Coupling scheme . . . . .	22
<b>4 Simulation cases</b>	<b>24</b>
4.1 Single Spout Bed simulation . . . . .	24
4.1.1 Geometry of the single spout bed . . . . .	24
4.1.2 Mesh and boundary conditions . . . . .	24
4.1.3 Physics Modelling and result extraction . . . . .	26
4.2 Heat transfer Simulation . . . . .	27
4.2.1 Numerical settings used for heat transfer model verification . . . . .	27
4.3 Spray Simulations . . . . .	27
4.3.1 Geometry of the Wurster Bed . . . . .	27
4.3.2 Mesh and Boundary conditions . . . . .	29
4.3.3 Physics Modelling and result extraction . . . . .	30

<b>5</b>	<b>Results and Discussion</b>	<b>32</b>
5.1	Single spout bed simulations . . . . .	32
5.1.1	Effect of fluid time step . . . . .	32
5.1.2	Momentum-Models . . . . .	33
5.1.3	Effect of rolling friction . . . . .	35
5.1.4	Effect of friction . . . . .	35
5.2	1D heat transfer simulations . . . . .	36
5.3	Spray simulations . . . . .	37
5.3.1	Wurster bed simulations . . . . .	37
5.3.2	Wurster bed spray simulations . . . . .	38
5.3.3	Correlation between particle radius and thickness of the film . . . . .	38
<b>6</b>	<b>Conclusion</b>	<b>41</b>
	<b>References</b>	<b>42</b>

## List of Figures

1.1	Schematic of the Wurster bed coating process along with different zones of interest. . .	4
1.2	Overview of the simulation software, IPS Fluidization <sup>TM</sup> , including the constituent parts: IPS IBOFlow©. . . . .	6
2.1	DEM iteration on a particle: (a) Identification of contacts, (b) Application of force on the particle, (c) Calculation of net reaction force, and (d) Particle displacement. . . .	10
2.2	DEM particle-collision Model . . . . .	11
2.3	Spray process from a spray cone injector, with R as the radius and A as the cone angle. . .	15
2.4	Different coupling mechanism: (a): Only fluid field affects the particles (b): Fluid filed affects the particles and vice-versa (c): Particle-Particle, Particle-Fluid and Fluid-Particle interaction. . . . .	16
3.1	Flowchart of the DEM Algorithm. . . . .	20
3.2	Different Particle arrangements as available in the IPS Fluidization. . . . .	20
3.3	A schematic representing the data transfer mechanism between the fluid solver (CPU) and the DEM solver (GPU). . . . .	22
3.4	Volume fraction calculation in split method . . . . .	23
3.5	Flowchart describing the coupling Algorithm used in IPS Fluidization <sup>TM</sup> . . . . .	23
4.1	Schematic of Single Spout bed. . . . .	25
4.2	Line probes location . . . . .	26
4.3	Schematic of the Wursted bed geometry representing different boundary regions. . . .	28
4.4	Sectional view of the Wurster bed along with the dimension. . . . .	30
5.2	Comparison of Momentum transfer coefficients . . . . .	33
5.3	Time averaged particle velocity for different momentum exchange models. . . . .	34
5.4	Vector plot of time averaged particle axial velocity plots for three different momentum-exchange models at the end of the simulation (4 sec). . . . .	35
5.5	Time averaged particle velocity for different values of rolling friction . . . . .	36
5.6	Time averaged particle velocity for different friction-coefficient . . . . .	36
5.7	Comparison of time evolution of temperature between the 1D simulation and IPSFluidization. . . . .	37
5.8	Comparison of time evolution of temperature for different fluid time steps. . . . .	37
5.9	Comparison of axial velocity from simulation with the experimental study of Li Liang et al. . . . .	38
5.11	Spray accumulation over time with varying flow rates . . . . .	40
5.12	Plot showing correlation between the radii of the particle and the spray accumulated for Nozzle Flow rate = 4.2m <sup>3</sup> /hr . . . . .	40

## List of Tables

4.1	Dimensions of the single spouted bed used in the simulations. . . . .	24
4.2	Particle settings used in the simulations. . . . .	25
4.3	Properties used in calculation of momentum transfer co-efficient for the verification study. . . . .	27
4.4	Wursted bed Dimensions . . . . .	29
4.5	Particle settings used in the Wurster simulations. . . . .	31
4.6	Moisture Properties used in the spray simulations. . . . .	31

# 1 Introduction

## 1.1 Physics of fluidized beds

Fluidization is a process in which the granular material is converted from a static solid-like state to a dynamic fluid-like state. This process occurs when a fluid (liquid or gas) is passed up through the granular material from the bottom of the bed. At low velocities, the aerodynamic drag of the particles is lower than the gravitational force, thus the bed remains in a fixed state. However, further increasing the velocity, increases the drag force on the particle causing the bed to expand in volume, making the particles to move away from each other. At a certain velocity, the aerodynamic force on the particles is balanced by the gravitational force causing the particles to become suspended within the fluid. At this point, the bed is said to be fluidized and it will exhibit fluidic behavior.

The devices using the property of fluidization are typically called fluidized beds. These beds possess excellent properties, such as a high surface area of contact between the fluid phase and solid particles per unit bed volume, high levels of intermixing of the particulate phase and frequent particle-particle and particle-wall collisions. This results in enhanced heat and mass transfer rates, high mixing rates and uniform reaction conditions. Hence, such devices have often been applied for processing applications such as coating, granulation, and drying. The application of fluidized beds, however, has been limited to relatively fine solids. This is because coarse materials when subjected to fluidization show a marked tendency toward slugging [1].

## 1.2 Physics of spouted fluidized beds

In order to overcome the limitation of fluidized beds, spouted beds were developed [2]. Such a bed comprises of a central nozzle with a high velocity jet, which results in a high velocity region in the central portion of the bed and a region with section of particles along the walls. As a result, the particles in the spout region move in a well structured manner in the vertical direction (with little radial displacement) accompanied by void (air bubble) propagation [3]. Mathur and Gishler [2] from their experimental studies found that the spout generation in the bed occurs only in a narrow range of gas flow rates. Nagarkatti and Chatterjee [4] reported that higher flow rates result in a lower contact time in the spout region. This is because, in the spouted bed, particles enter the spout radially from the bottom and travel to the top and subsequently fall down in the bottom annulus region. The radial flow of particles in this system is limited as a result there is a non uniform distribution of particles at higher flow rates and results in the formation of dead zones where particle do not interact with the flow. This disadvantage was overcome by using a spouted fluidized bed [5]. In addition to the flow from the central nozzle, such beds comprise of an additional background gas flow (also known as auxiliary or fluidizing gas). Such beds have the combined features of both the fluidized and the spouted beds. This, in turn, leads to higher circulation and mixing rates, due to the bubble generation, leading to enhanced particle movement in vertical and radial directions. This action prevents the formation of slugs and results in a well defined particle circulation pattern. As a result, these beds possess excellent mixing rates, favorable reaction conditions, and exceptional heat and mass transfer characteristics. Hence they are well suited for application involving drying, coating, granulation such as powder coating of pellets [6–10].

### 1.3 Modeling of spouted fluidized beds

From a macroscopic point of view, the solid phase in a fluidized bed behaves like a fluid. Thus, most of the earlier simulations of the fluidized bed were based on theories that treated the solid phase as a continuum, such as the two-fluid model [11]. However, it later became computationally feasible to track individual particles, following the development of the Discrete Element Method (DEM) [12]. In this method, the mechanics of collisions between two particles are modeled using a soft sphere approach as first suggested by Cundall and Strack [13]. Rapid progress in the field has led to using improved gas-particle and particle-particle models for spouted fluidized bed, typically known as Computational Fluid Dynamics-Discrete Element Method (CFD-DEM). In the CFD-DEM approach, the gas phase is considered as a continuum phase and treated using a Eulerian approach while the DEM phase is treated as a discrete phase based on the Lagrangian approach. The two phases interact through a momentum exchange term. As this method is computationally expensive, the number of particles that could be simulated has typically been very limited. However, due to the steadily rising increase in computational power, the number of particles that can be simulated has recently increased significantly. As an example, Buijtenen *et al.* [14] performed pseudo 2-D simulation on single and multiple spout bed using CFD-DEM modeling technique using a four way coupling approach (particle-particle, particle-wall, particle-fluid, and fluid-particle) with a maximum of 100,000 particles. Sutkar *et al.* [3] showed that using the graphics processing unit (GPU) for running CFD-DEM simulation could effectively increase the number of particles that could be simulated where they simulated a maximum of 25,000,000 particles in a simplified geometry.

Heat transfer between the particles and the gas phase is essential in various processes, including drying and coating, for which the efficiency of heat transfer is crucial. For example, in the pharmaceutical industry, the drying rate influences the thickness of the coated film over the pellets, which in turn impacts the rate of drug release in the human body [15, 16]. As an another example, in the agriculture industry, drying of seeds is widely adopted to increase their shelf life. Overexposure of the seeds to excessive heat can cause thermal damage of grains [8]. This has resulted in an intense research initiative to find reliable models for capturing the essential heat transfer characteristics of a fluidized bed. Patil *et al.* [17] studied the heat transfer from a hot air stream to the particles. They extended the CFD-DEM model with the heat transfer model where the continuous phase is modeled using a convection-diffusion equation while the discrete phase is modeled using a thermal energy equation for each individual particle. They studied the effect of the inlet temperature and the particle size on the size of the bubble formed in the fluidized bed. Similarly, Patil *et al.* [18] studied the effect of hot gas injection into a particulate bed at minimum fluidization velocity and evaluated the heating and thermal equilibrium of particles with incoming gas. The mentioned study, varied the the number of particles that were simulated based on the size of the particles, with a maximum of 700,000 particles simulated for a diameter of 1mm. Tsory *et al.* [19] incorporated models for conductive heat transfer between particle-particle, particle-wall and convective heat transfer between particles and fluid. Through their study, they evaluated the effect of particle roughness on heat transfer, with simulations limited to 25000 particles. Wu *et al.* [20] included complete models considering particle motion, fluid flow, particle-fluid interactions, and heat convection, conduction and particle radiation for packed pebble beds and explored the effect of particle thermal radiation on the flow and heat transport characteristics in a packed pebble bed.

In processes such as coating and particle granulation in addition to the heat transfer, there is a need for a spray model. The coating solution used in the spray process consists of a mixture of liquid (solvent) and solid (solute). In such processes, the coating solution is made to spray over the particles. The solute sticks to the particle and the solvent evaporates due to heat from the background air resulting in the formation of a solid layer around the particle. Such a coating process is widely carried

out in Wurster beds.

The image of a Wurster bed is shown in Figure (1.1). The Wurster bed consists of several regions, the spray zone, the Wurster column, the horizontal transport region, and the fountain region. The particles enter the spray zone through the Wurster column where they collide with the droplets. The coated particles get dried by the background air and the dried particles settle down at the bottom of the bed in the horizontal transport region. These particles are subjected to the same cycle repetitively. The time taken by a particle to complete one cycle is called the cycle time.

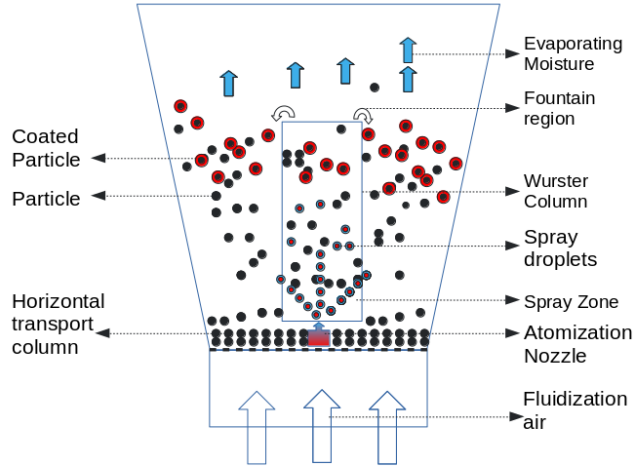


Figure 1.1: Schematic of the Wurster bed coating process along with different zones of interest.

A process like the particle granulation and coating is sensitive to changes in operating conditions. For example, the balance between the evaporation rate and the liquid injection rate is delicate. If the liquid injection rate is too high in comparison to the evaporation rate it can lead to excess agglomeration of particles. However, if the evaporation rate is too high, relative to the injection rate there is a formation of vapor layer around the particle, which prevents the liquid from sticking to the surface of the particle (non-wetting contact). As a result of this, heat flux near the surface decreases despite high temperature gradient across the surface [21].

Sutkar *et al.* [22] developed a model for combined heat and mass transfer with liquid injection in which both the particles and the droplets are considered as a discrete phase. In their study, they considered the assumption that the collision between the droplet and particle results in a uniform layer of coating around the particle. The number of particles that were simulated, in this case was 82505. Askarishahi *et al.* [21] modeled liquid injection using the Euler-Lagrangian approach in which the droplets were treated as a continuous phase and the particle as a Lagrangian phase. In this model, they incorporated the effect of cooling of the air stream due to the evaporation of droplets from the particle surface and that of suspended droplets. The surface coverage model did not consider a uniform approach as that of models used by [22] and the coverage model used was that of Kariuki *et al.* [23]. In their study, the number of particles that were simulated varied from 60,000 to 1,000,000.

A full scale spray simulation for a coating process comprises a complex interplay of the various physical phenomenon. Since such a simulation requires extensive use of computational resources along with the need for selecting for suitable models for spray, heat, and the DEM, the number of particles that have been simulated is limited to few thousand particles. The thesis aims to investigate the process in detail by conducting simulations on a large scale with more than a million particles.

## 1.4 Purpose of the project

In the current project, the in-house developed CFD-DEM tool IPS Fluidization<sup>TM</sup> from Fraunhofer Chalmers Centre (FCC) is used to simulate the spouted fluidized bed process, including both heat transfer and a spray phase with evaporation. The software is a state-of-the-art simulation tool with strong focus on HPC and efficient utilization of both the CPU and the GPU. The constituents of the software is further described below as in Section 1.5. The purpose of the current project was not on the implementation of the tool, but on the application of the tool.

The project is focused on verification and validation of the tool, as well as investigations of the current practical limits in terms of computational time and system sizes possible to simulate. The verification is performed in terms of running the software to investigate the previous implemented features of the code, including investigations of the influence of different fields of physics. Wherever possible, validations are performed against experimental studies from the open literature (for which the availability is further discussed below, Section 1.6).

The main target of the software is currently to simulate the pellet coating process for the pharmaceutical industry using the mentioned software. In relation to this, the current thesis investigates the feasibility to study an actual experimental setup for pellet coating process comprises of millions of particles. Whereas in the open literature the maximum number of particles that were simulated in a drying process was limited to 1 million particles with the spray droplets treated as a continuum phase [21], the goal for the current thesis is thus to stretch beyond the mentioned simulation sizes, and also include a more detailed Lagrangian treatment of the spray parcels as done by IPS Fluidization<sup>TM</sup>.

In summary, the main objectives of the project are to:

- Model and perform CFD-DEM simulation of a few thousand particles using IPS Fluidization for the purpose of validating the solver based on experimental data available in the literature.
- Investigate the coupling between the fluid and the particle using different momentum exchange models, convergence studies of the fluid time step and to identify the key parameters influencing the particle motion in the bed, including friction and rolling friction.
- Perform verification studies on the heat transfer model in IPS Fluidization
- Model and perform industrial scale simulation for the purpose of studying the variation of characteristics of the coated film with the different size distribution of particles.

## 1.5 Simulation software

The simulation software IPS Fluidization<sup>TM</sup> is a tool combining the state-of-art CFD multiphase solver IPS IBOFlow© [24, 25] and an in-house DEM solver, both developed by FCC. IBOFlow© has previously been used to successfully simulate a number of different industrial applications, such as fiber suspension flow [26, 27], rotary bell spray simulation [28, 29], sealing applications [30, 31], 3D bioprinting [32] and cases where surface tension play a pivotal role [33]. The in-house DEM solver is a state-of-art solver for both spherical particles and complex shape particles such as rock fragments. The tool include support for arbitrary triangulated domains with models for a range of physical interactions. The solver is implemented for massive parallelization on the GPU, with a linear scaling of the solver well above 10 million particles.

IPS Fluidization<sup>TM</sup> contains a coupling layer which treats the data exchange between the Lagrangian

phases (the particles and the spray droplets) and the continuum fields (gas and moisture) in an efficient manner. The data exchange is performed on a generalized grid which is independent of the fluid computational mesh. Due to efficient handling of particle collisions and data interpolation, the transfer between the GPU (particles and spray) and the fluid fields is minimized. The latter allows for a high-resolution coupling with a minimal overhead in terms of simulation time. A schematic of the solver is presented in Figure 1.2.

The user interface is implemented via a domain specific language based on Lua. The user sets up and models the problem in a combined approach, making the user completely agnostic to the underlying recipient of the parameters (DEM or CFD). The Lua layer allows for dynamic result extraction via probes, line extraction and also complete data files using the H5 format.

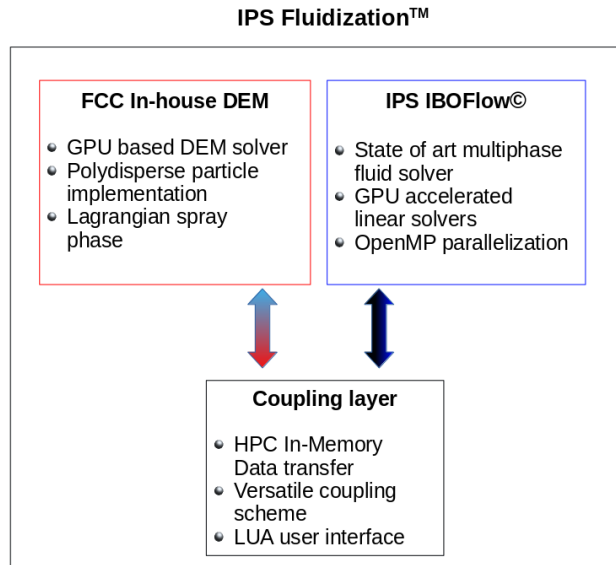


Figure 1.2: Overview of the simulation software, *IPS Fluidization™*, including the constituent parts: *IPS IBOFlow©*.

## 1.6 Experimental Data

In this section, the experimental validation data available in the open literature are discussed. It should be noted that extensive validation has previously been done at FCC for the separate solvers of *IPS Fluidization™*, and thus the primary aim for the thesis is to find validation data for the coupled solver.

For validation of momentum transfer between the particles and the fluid, the experimental studies conducted on a single spout bed by Buijtenen *et al.* [14] was considered. The study collected the time-averaged particle velocity fields for the spout-fluidization regime measured using particle image velocimetry (PIV) and positron emission particle tracking (PEPT). As such, the data series has been used extensively in the literature for validation of DEM-CFD solvers [3, 34, 35].

For the heat transfer and the spray models there is an apparent lack of experimental data in the literature. In many cases the mentioned fields of physics are only verified in qualitative manner [17, 18, 21, 22]. Hence, the current project is restricted to verifying the cases using simple 1D models as a basis.

As a preparatory step for the industrial scale simulation, a validation of the input parameters that are needed for a large scale pilot simulation, studies are performed on a small scale setup based on the experimental studies conducted by Liang *et al.* [36].

## 1.7 Structure of the thesis

The rest of the chapters in this thesis are structured as follows

- In Chapter 2, the different CFD and DEM models along with their coupling scheme are presented.
- In Chapter 3, the DEM-CFD methodology and the coupling strategies are discussed.
- In Chapter 4, the description of various simulation cases are given.
- Finally, in Chapter 5, the results of various simulations are presented and discussed.

## 2 Theory

The CFD-DEM method is used to model systems comprising of a fluid and a solid phase (for early uses of the method see e.g. developed by Tsuji *et al.* [12]). The fluid phase is solved using the CFD technique, in which the gas phase is treated as a continuum phase based on the Eulerian approach, with conservation equations formulated for all fields of physics (Section 2.1).

The particles are considered as a discrete phase and treated based on the Lagrangian approach and solved using DEM. In this approach, each particle is tracked individually and their positions, velocities, etc are described as a function of time. Furthermore, the collisions between particles and particles and walls are resolved in a so-called soft sphere manner. The DEM approach is further described in Section 2.2. In addition, the Lagrangian droplet phase is described in Section 2.3.

Since the fluid phase and solid phase are treated in different mathematical frames of references, the coupling terms are of profound importance in CFD-DEM. In general, the coupling between the fluid and the solid phase happens in a two way approach, i.e., the fluid field influences the particles and particles, in turn, affects the fluid. The coupling between the particles and fluid is further described in Section 2.4.

### 2.1 Computational Fluid Dynamics

Computational Fluid Dynamics is the analysis of systems involving fluid flow, heat transfer and associated phenomena with the help of computers. This method comprises of three main steps which are described below [37].

- Integration of the governing equations of fluid flow over all the (finite) control volumes of the domain.
- Discretization – conversion of the resulting integral equations into a system of algebraic equations.
- Solution of the algebraic equations by an iterative method.

Thus it is essential to describe the governing equations for the gas phase dynamics before it could be discretized into algebraic equations. For the current applications, the gas phase is treated as an incompressible Newtonian fluid. The model for the gas phase is described using the volume averaged Navier-Stokes equations, where all variables are locally averaged over the control volume. These equations describe how the velocity, pressure, temperature, and density of a moving fluid are related.

#### 2.1.1 Mass and momentum conservation

The governing equation for the conservation of mass is given by the continuity equation as follows,

$$\frac{\partial(\epsilon_f \rho_f)}{\partial t} + \nabla \cdot (\epsilon_f \rho_f \mathbf{u}_f) = 0. \quad (2.1)$$

Newton's second law states that the rate of change of momentum of a fluid phase equals the sum of the forces on the particle. The forces may be surface forces or body forces. The governing equation describing the action of such forces on the fluid phase is given by the momentum equation. The momentum equation for the fluid phase is given as follows [34],

$$\frac{\partial \epsilon_f \rho_f \mathbf{u}_f}{\partial t} + \nabla \cdot (\epsilon_f \rho_f \mathbf{u}_f \mathbf{u}_f) = -\epsilon_f \nabla p - \nabla \cdot (\epsilon_f \boldsymbol{\tau}_f) + \mathbf{S}_p + \epsilon_f \rho_f \mathbf{g}, \quad (2.2)$$

where  $\rho_f$  is the density of the gas phase,  $\tau_f$  is the gas phase stress tensor,  $\mathbf{u}_f$  is the velocity of the gas phase and  $\mathbf{g}$  is the gravitational acceleration constant. The gas phase stress tensor is calculated as follows,

$$\tau_f = -\mu_f \left( (\nabla \mathbf{u}_f) + (\nabla \mathbf{u}_f)^T \right) + \frac{2}{3} \mu_f \nabla \cdot \mathbf{u}_f \delta, \quad (2.3)$$

where  $\mu_f$  denotes the viscosity of the gas phase.  $\mathbf{S}_p$  denotes the source term for coupling the momentum transfer from the particulate phase and will be described in detail in the coupling section (Section 2.4).

### 2.1.2 Heat transfer

Since the process of particle coating involves drying of the solvent that is deposited over the particle phase it is essential to include models for heat transfer. The applied thermal energy equation for the gas phase as proposed by Syamlal and Gidaspow [38] is given by:

$$\frac{\partial(\epsilon_f \rho_f C_{p,f} T)}{\partial t} + \nabla \cdot (\epsilon_f \rho_f \mathbf{u}_f C_{p,f} T) = \nabla \cdot (\epsilon_f k_f \nabla T) + S_h, \quad (2.4)$$

where  $S_h$  represents the source term for heat coupling with the particulate phase and will be described in detail in Section 2.4.2.  $C_{p,f}$  is the fluid heat capacity and  $k_f$  is the thermal conductivity of the gas phase.

### 2.1.3 Moisture conservation equation

The particles are moistened when hit by the spray droplets. Due to the heated fluidization air, the solute evaporates from the particles and is convected by the air. The conservation equation describing the transport of the moisture ( $w_f$ ) is given by [22],

$$\frac{\partial \epsilon_f \rho_f w_f}{\partial t} + \nabla \cdot (\epsilon_f \rho_f \mathbf{u}_f w_f) = -\nabla \cdot (\epsilon q_m) + S_m, \quad (2.5)$$

where the term  $q_m$  represents the mass transfer flux which is described in terms of the gas diffusivity ( $D_f$ ) such that:

$$q_m = D_f \nabla w_f, \quad (2.6)$$

and  $S_m$  is the source term for coupling the mass transfer between fluid and the particulate.

## 2.2 Discrete Element Method

DEM is a particle-scale numerical method for modeling the bulk behavior of granular materials [13]. Each particle is represented by its specific properties such as its size, shape, velocity and angular velocity. The particles are subjected to forces due to gravity, momentum exchange with the fluid, particle-particle interaction and particle-wall contact forces. The trajectories of the particles are explicitly solved using Newton's second law of motion under small incremental steps in time. In practical terms, this requires solving one ODE per state variable (position, velocity and angular velocity) and per time step.

The process is represented in Figure (2.1). In Figure (2.1), a particle tends to come in contact with other particles, as a result, it experiences force from other particles. Forces from fluid phase and gravity are also included in this step. The net force acting on the particle is calculated and the particle state is updated using Newton's second law.

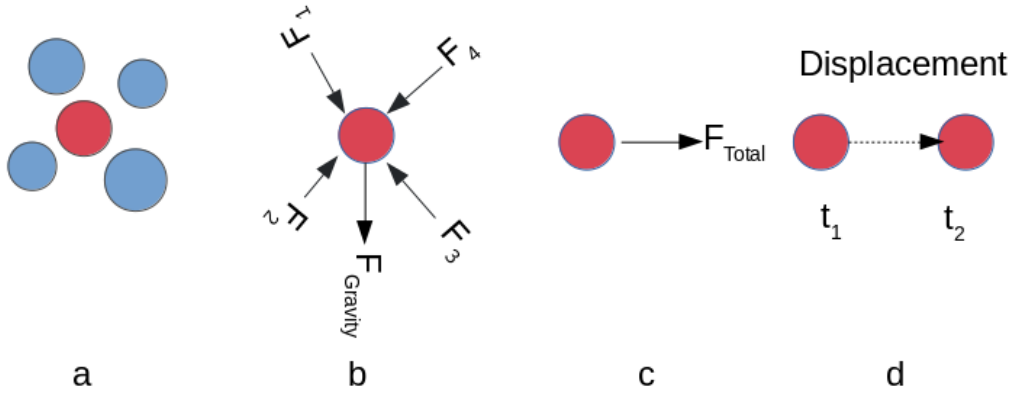


Figure 2.1: *DEM iteration on a particle: (a) Identification of contacts, (b) Application of force on the particle, (c) Calculation of net reaction force, and (d) Particle displacement.*

### 2.2.1 Particle Governing Equation

The equation describing the motion of particle based on Newton law with relevant forces in a fluidized bed as modeled by Buijtenen *et al.* [39] on spouted fluidized beds is given as follows,

$$m_p \frac{dv_p}{dt} = -V_p \nabla p + \frac{V_p \beta}{1 - \epsilon_f} (\mathbf{u}_f - \mathbf{v}_p) + m_p g + \sum_{\forall b \in N_p} F_{a \leftrightarrow b} + \sum_{\forall b \in N_w} F_{a \leftrightarrow b}, \quad (2.7)$$

where each term in the above equation is described in detail in the following sections. The first two terms on the right hand side represents the force felt by the particle in the presence of the fluid field.

#### Pressure gradient force

The pressure fields in the flow undisturbed by the presence of the particle contribute to the force on the particle. This force is typically small and is neglected in gas-solid flows.

#### Drag force

The force acting opposite to the relative motion of any object moving with respect to a surrounding fluid results is called as drag force. Some of the factors that influence the drag force are the shape, size of the particle,

In addition to these forces, a particle might also experience other forces such as lift, virtual mass, and the Basset force. However, these force are quite small and are neglected in gas-solid flows, which is the primary interest in this study.

#### Gravitational force

The third term on the right side of the Equation 2.7 is the gravitational force. This term depends on the mass of the particle and is the main force responsible for the downward movement of the particle in the bed.

## Particle-particle interaction force

The fourth term on the right side of the Equation 2.7 represents the particle-particle interaction force. In dense flows, the loss of kinetic energy by inter-particle collisions is high and hence, it is important. The soft sphere model developed by Cundall and Strack [13] is typically applied in DEM. This model treats particle-particle collisions as finite overlaps. In this model, particles are typically assumed to remain geometrically rigid during contact. The deformation of the particle during the collision is assumed to be small.

The contact force is modeled based on an equivalent of the spring and a dash-pot system. The elastic part contact force is modeled by the spring, while the inelasticity is represented by the dash-pot. An additional sliding element is placed in series with the spring mass damper in the tangential direction to recover the effect of friction.

Spring constants and damping coefficients in the normal and tangential directions are used to calculate the normal and tangential forces respectively, due to the particle overlaps. Such a system is shown in Figure 2.2.

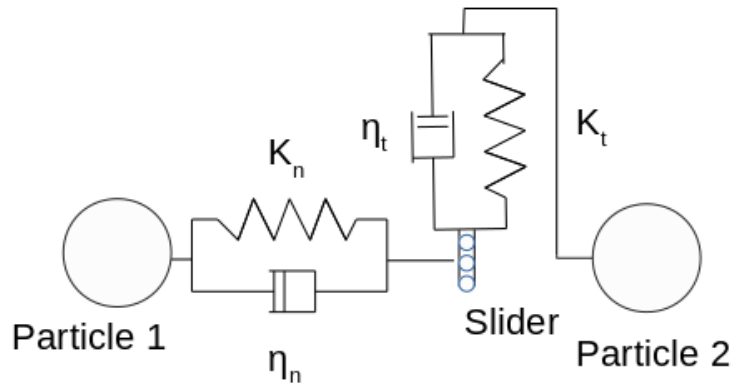


Figure 2.2: *DEM particle-collision Model*

The normal force between two collisions is calculated based on the normal overlap of the spheres such that,

$$f_{n,12} = -K_n \delta_{n,12} - \eta_n v_{n,12}, \quad (2.8)$$

where the term  $f_{n,12}$ ,  $\delta_{n,12}$  and  $v_{n,12}$  denotes the normal force, normal particle overlap and normal relative velocities between particle 1 and particle 2 respectively. The terms  $K_n$  and  $\eta_n$  represents the normal spring constant and normal coefficient of viscous dissipation respectively.

The tangential direction spring stiffness is generally history dependent and computed in terms of a fictitious tangential deformation of the sphere (see e.g. [40]). However, for performance reasons, a simplified model model is applied for the tangential direction, avoiding the history effect but still recovering the effect of the friction (see e.g. [34]).

The normal and tangential stiffness constant are calculated based on HMDns model. The HMDns model is a combination of Hertzian model [41] of normal stiffness and the no-slip theory of Mindlin

[42] for the tangential stiffness. The normal stiffness in this model is given as follows,

$$k_n = \frac{4}{3}E^* \sqrt{R\delta_n}, \quad (2.9)$$

where the term  $E^*$  is calculated as follows,

$$E^* = \frac{E}{2(1 - \nu^2)}, \quad (2.10)$$

based on Young's modulus ( $E$ ) and Poisson's ratio ( $\nu$ ). The stiffness of the particles also affects the spring force and the collision time.

The last term on the right side of the Equation 2.7 represents the interaction force between the wall and the particle. This interaction is treated in the same way as particle-particle interaction, with the wall having zero velocity.

The particle also experiences rotation in a bed in addition to translation. This is given by the angular momentum equation, one main assumption in this equation is that the torque is solely due to particle-particle contact and not due to fluid-particle interaction. The equation describing the rotation of a spherical particles is given as follows,

$$I_p \frac{d\omega_p}{dt} = \sum_{N_p} \mathbf{M}_p, \quad (2.11)$$

where  $\omega_p$  is particle angular velocity,  $M_p$  is the torque, and  $I_p$  is the moment of inertia.

In addition to the above described forces, the model also includes a rotational friction term giving rise to a momentum on the particle such that[43]:

$$M_r = -\frac{\omega_{rel}}{|\omega_{rel}|} \mu_r R f_n \quad (2.12)$$

where  $\omega_{rel}$  is the relative rotational velocity between two particles or between a particle and the wall. The induced moment contributes to  $\mathbf{M}_p$  above.

## 2.2.2 Heat transfer Model

Various modes of heat transfer manifest in a system with gas-solid flows. The particulate phase, in principal experiences particle-particle and particle-wall heat conduction, convective heat transfer with the surrounding gas, particle-particle/wall frictional heating and radiative heat transfer with the surrounding gas and bed walls. Heat transfer through radiation is significant only for high temperatures (typically  $> 700$  K). The mode and the rate of heat transfer are dependent on the system of application and its flow characteristics and the following assumptions are considered here:

- Conductive heat transfer between particle-particle and particle-wall were neglected. This assumption is valid if particles are in free flight all the time which is true in case of fluidized systems.
- Radiative heat transfer is neglected as the absolute temperature is relatively low (less than  $100^\circ\text{C}$ )

Base on those assumptions, the heat balance equation for a particle p, as used by Patil *et al.* [17] in their work on heat transfer is given as follows,

$$\rho_p V_p C_{p,p} \frac{dT_p}{dt} = h_{fp} A_p (T_f - T_p), \quad (2.13)$$

where  $T_f$  is the fluid temperature,  $A_p$  is effective area of the particle available for heat transfer and  $C_{p,p}$  is the particle heat capacity. This equation incorporates heat transfer between fluid and gas phase through convection. The term  $h_{fp}$  represents the heat transfer co-efficient between the gas and the particles evaluated using the empirical Nusselt number correlation as given by Gunn [44],

$$Nu_p = (7 - 10\epsilon_f + 5\epsilon_f^2)[1 + 0.7Re_p^{0.2}Pr^{0.33}] + (1.33 - 2.40\epsilon_f + 1.20\epsilon_f^2)Re_p^{0.7}Pr^{0.33}, \quad (2.14)$$

where the terms  $Re_p$  and  $Pr$  denote the particle Reynold's number and Prandtl number respectively. They are calculated as follows,

$$Re_p = \frac{\rho_f \epsilon_f d_p |\mathbf{u}_f - \mathbf{v}_p|}{\mu_f}, \quad (2.15)$$

$$Pr = \frac{\mu_f C_{pf}}{k_f}, \quad (2.16)$$

and the term  $Nu_p$  is the Nusselt number (which is the ratio of convective to conductive heat transfer at a boundary in a fluid) is used to calculate heat transfer co-efficient as follows,

$$h_{fp} = \frac{Nu_p k_f}{d_p}. \quad (2.17)$$

### 2.2.3 Mass transfer model

In the current application, the spray phase is, after deposition on the particles, evaporated from the particle surface to the surrounding fluid. The driving force for evaporation is the difference in concentration of the droplet vapor between the particle surface and the free stream. Under the current assumption of a uniform layer of spray solid and spray liquid over the particle, the equation describing the transfer of mass from the liquid phase to the gas phase is given as follows [22],

$$\frac{dm_p}{dt} = k_m A_p (w_f^* - w_f), \quad (2.18)$$

where the term  $k_m$  denotes the mass transfer coefficient for the gas phase which is a proportionality constant that relates the mass transfer rate and change in concentration of moisture content as driving force. Further, the term  $w_f^*$  denotes the saturated concentration of liquid at the solid-liquid interface. In a two component system, a thermodynamic equilibrium exists at the gas-liquid interface. Hence, the term  $w_f^*$  at the interface can be calculated as follows,

$$w_f^* = \frac{m_d X_{d,s}}{m_d X_{d,s} + m_f (1 - X_{d,s})}, \quad (2.19)$$

where  $X_{d,s}$  is the mole fraction of moisture at the particle surface  $m_f$  and  $m_d$  are the molecular weights of surrounding gas and surrounding droplet respectively. The mole fraction of moisture at the particle surface is described by Clausius Clapeyron equation, by assuming a thermodynamic equilibrium at the gas-liquid interface. The term is given as follows,

$$X_{d,s} = \frac{P_{ref}}{P_{amb}} \exp\left(\Delta H_{atm} \left(\frac{1}{T_{b,atm}} - \frac{1}{T_{d,s}}\right) \frac{m_d}{R}\right), \quad (2.20)$$

and is calculated based on ambient pressure  $p_{amb}$  and the reference  $p_{ref}$  with  $\Delta H_{evap}$  being the evaporation enthalpy defined at reference pressure and the boiling temperature at reference pressure  $T_{b,ref}$ ,  $R$  is the universal gas constant and  $m_d$  is the molar mass of the moisture.

The effect of a relative velocity between the droplet and the conveying gas is to increase the evaporation or condensation rate. This effect is represented in [44] using the Sherwood correlation as follows,

$$Sh_p = (7 - 10\epsilon_f + 5\epsilon_f^2)[1 + 0.7Re_p^{0.2}Pr^{0.33}] + (1.33 - 2.40\epsilon_f + 1.20\epsilon_f^2)Re_p^{0.7}Sc^{0.33}, \quad (2.21)$$

where  $Sc$  being the Schmidt number is used to characterize fluid flows in which there is simultaneous momentum and mass diffusion convection processes calculated based on the viscosity, density and diffusivity of the gas phase as follows,

$$Sc = \frac{\mu_f}{D_f \rho_f}. \quad (2.22)$$

The mass transfer coefficient is evaluated based on the Sherwood number correlation calculated based on the Equation 2.21, gas diffusivity  $D_f$  and particle diameter as follows,

$$K_m = \frac{Sh_p D_f}{d_p}. \quad (2.23)$$

## 2.3 Spray droplets

The spray droplets are a mixture of spray solid and the spray fluid. The purpose of having the spray in the simulation is to simulate the coating process. Since the individual collision between the particles and the droplets needs to be resolved it is essential to track the droplets in a Lagrangian sense. In the current framework, the collisions between the droplets are not resolved, i.e., no two droplets collide with each other. Furthermore, the spray is currently assumed to have a one way interaction with the gas phase, i.e., the droplets experience the force from the fluid through the momentum exchange term. However the presence of droplet does not affect the gas phase itself. Such an assumption is valid under low spray loadings.

Further, the droplets are simulated under the assumption of low droplet Weber number, such that any breakage of the droplets can be neglected. This assumption is reasonable since most droplet breakage takes place in a very small region close to the nozzle, after which the droplets are small enough to keep their size. The characteristic sizes of the droplets are to be chosen based on size representable for the spray after the initial breakup.

In a droplet particle collision, it is assumed that the droplets are completely captured by the particles. This assumption is valid in cases with a small droplet to particle diameter ratio. As mentioned above, a captured droplet is assumed to form a uniform liquid layer around the particle. In the current approach, the droplets will not alter the characteristics of the particles, e.g, not increasing the mass of the particles, which is reasonable for small spray loadings applied under a short simulation time. Finally, it is assumed that the droplets have the same temperature as that of the gas phase and also there is no evaporation from the droplets present in the gas phase, which is again a reasonable assumption if the time from injection to collision is short.

An outline of the spray process is shown in Figure 2.3. The droplets are a mixture of a spray solid (red colour) and spray liquid (blue colour). When the droplets collide with the particles (black colour) they droplets are removed from the simulation in the gas phase and get deposited on to the particle. The moisture evaporates and the coating (spray-solid) is left on the particles.

## 2.4 Multiphase Coupling

As touched upon in the previous sections, the fluid and the particles are coupled via the exchange of momentum, energy and mass.

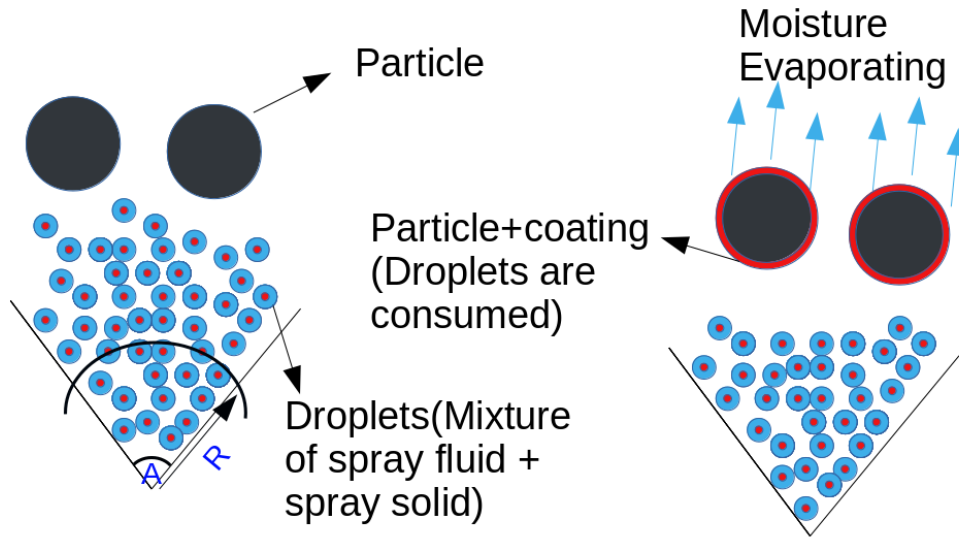


Figure 2.3: *Spray process from a spray cone injector, with  $R$  as the radius and  $A$  as the cone angle.*

In general, a coupling between the particles and the gas depends on the particle size, the relative velocity and the volume fraction of the solid phase. From an exchange point of view there are three typically considered classes of problems:

- One way coupling: This type of coupling is mainly present in sufficiently dilute flows such that fluid feels no effect from the presence of particles. In this type of flow, particles move in dynamic response to the fluid motion (See Figure 2.4.a).
- Two way coupling: If enough particles are present in the fluid phase, such that the momentum exchange between dispersed and carrier phase interfaces alters dynamics of the carrier phase, it is essential to model a two way coupling between the carrier phase and the particle phase (See Figure 2.4.b).
- Four way coupling: If the flow is dense enough, the effect of dispersed phase collisions are significant. In such a situation there is a need for four way coupling. In a four way coupling, the fluid field affects the dispersed phase, the dispersed phase in turn affect the fluid, in addition to that, there is an interaction between the dispersed phase (See Figure 2.4.c).

The three types of coupling mechanism are shown in the Figure 2.4,

In a system such as the fluidized bed, there is interaction between the dispersed phase, as well as interaction with the fluid phase, essentially requiring four way coupling. The coupling between the particle-particle and particle-wall interaction is described in the Section 2.2.1. In this section, different interphase coupling mechanism such as the momentum, energy and mass will be described in detail.

### 2.4.1 Momentum Exchange

The coupling between the fluid and the dispersed phase happens through the interphase momentum exchange term in the momentum Equation 2.2 for the fluid and for the particle Equation 2.7. In order to couple the fluid and the dispersed phase, it is essential to calculate the volume fraction of particle present in each cell. The particle volume fraction is calculated by measuring the fraction of

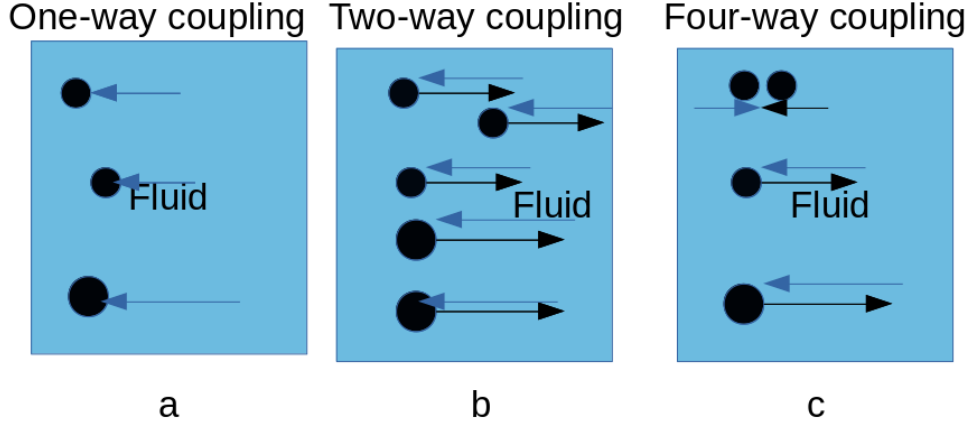


Figure 2.4: *Different coupling mechanism: (a): Only fluid field affects the particles (b): Fluid field affects the particles and vice-versa (c): Particle-Particle, Particle-Fluid and Fluid-Particle interaction.*

the particle present in a cell as follows,

$$\epsilon_{p,cell} = \frac{\sum_{\forall i \in cell} f_{cell}^i V_p^i}{V_{cell}} \text{ if } \epsilon_{p,cell} < 1, \quad (2.24)$$

where the  $f_{cell}^i$  is the volume fraction of particle  $i$ , belonging to a particular cell and  $V_p^i$  is the volume of the  $i^{th}$  particle belonging to the cell. The source term for the coupling between the phases is calculated as follows,

$$\mathbf{S}_p = \frac{1}{V_{cell}} \sum_{\forall i \in cell} f_{cell}^i \beta_p^i V_p^i (\mathbf{u}_f - \mathbf{v}_p^i). \quad (2.25)$$

The term  $\beta$  is the momentum transfer co-efficient. There are a multitude of models for calculating the momentum transfer co-efficient. However the most predominantly used models in the literature [3, 14, 18, 35, 39] for studying fluidized beds are the correlations developed by a combination of by models Ergun [45] (model 1) and Wen and Yu [46] (model 2) which will be represented as Ergun-Wen-Yu model, Koch-Hill [47] and Beetstra [48]. The drag model is an important parameter in gas-solid interaction modeling as it allows to determine the momentum transfer between the gas and solid phases. The description of the moment transfer through the drag model is very important, since fluidization is a result of the drag exerted by the interfacial gas flow on the particles. The comparison of different drag models as done in [49] showed that the Koch-Hill, Beetstra and Ergun-Wen-Yu models were able to predict hydrodynamic parameters of gas-solid flow in a fluidized bed more effectively than other models.

The formulation for calculating these coefficients are given below as follows.

The drag co-efficient  $\beta$  in the Ergun-Wen-Yu model is a combination of momentum coefficient evaluated at different flow regimes. The coefficient is formulated by Ergun [45] for the dense regime and by Wen and Yu [46] for the dilute regime. It is given as follows,

$$\beta_{Ergun-Wen-Yu} = \begin{cases} 150 \frac{(1 - \epsilon_f)^2 \mu_f}{\epsilon_f d_p^2} + 1.75 \frac{\rho_f (1 - \epsilon_f) |\mathbf{u}_f - \mathbf{v}_p|}{d_p} & \text{if } \epsilon_f \leq 0.8 \\ \frac{3}{4} C_d \frac{\rho_f (1 - \epsilon_f) \epsilon_f^{-2.65} |\mathbf{u}_f - \mathbf{v}_p|}{d_p} & \text{if } \epsilon_f > 0.8, \end{cases} \quad (2.26)$$

where  $C_d$  is the drag coefficient formulated based on the particle Reynolds's number as follows,

$$C_d = \begin{cases} \frac{24}{Re_p}(1 + 0.15Re_p^{0.687}) & (Re_p \leq 1000) \\ 0.44 & (Re_p > 1000). \end{cases} \quad (2.27)$$

The momentum transfer coefficients due to drag as given by Hill *et al.* [47], is calculated using a drag relation proposed by Koch and Hill (2001) again based on lattice-Boltzmann simulations which works in the same Reynolds's number range as 1000 as given in [48]. It is given as follows,

$$\beta_{Koch-Hill} = \frac{18\mu_f\epsilon_f^2(1-\epsilon_f)}{d_p^2} \left( F_0 + \frac{1}{2}F_3Re_p \right), \quad (2.28)$$

where the coefficients  $F_0$  and  $F_3$  are based on the fluid volume fractions. The term  $F_0$  is calculated as follows,

$$F_0 = \begin{cases} \frac{1 + 3\sqrt{\frac{(1-\epsilon_f)}{2}} + \frac{135}{64}(1-\epsilon_f)\ln(1-\epsilon_f) + 16.1(1-\epsilon_f)}{1 + 0.68(1-\epsilon_f) - 8.48(1-\epsilon_f)^2 + 8.16(1-\epsilon_f)^3} & \text{if } (1-\epsilon_f) < 0.4, \\ \frac{10(1-\epsilon_f)}{\epsilon_f^3} & \text{if } (1-\epsilon_f) \geq 0.4 \end{cases}, \quad (2.29)$$

and the term  $F_3$  is calculated as follows,

$$F_3 = 0.0673 + 0.212(1-\epsilon_f) + \frac{0.0232}{\epsilon_f^5}. \quad (2.30)$$

The momentum transfer coefficient as given by Beetstra *et al.* [48] was formulated based on the lattice Boltzmann simulations. This model works well upto a Reynolds's number range of 1000 which is the same as in Koch-Hill model.

$$\beta_{Beetstra} = K_1\mu_f \frac{(1-\epsilon_f)^2}{d_p^2\epsilon_f} + K_2\mu_f \frac{\epsilon_p Re_p}{d_p^2}, \quad (2.31)$$

where  $K_1$ ,  $K_2$  are coefficients which are dependent on the volume fraction of the two phases and the Reynolds's number given as follows,

$$K_1 = 180 + 18 \frac{\epsilon_f^4}{\epsilon_p} (1 + 1.5\sqrt{\epsilon_p}), \quad (2.32)$$

$$K_2 = 0.31 \frac{\epsilon_f^{-1} + 3\epsilon_f(1-\epsilon_f) + 8.4Re_p^{-0.343}}{1 + 10^{3(1-\epsilon_f)}Re_p^{2\epsilon_f-2.5}}. \quad (2.33)$$

## 2.4.2 Energy exchange between the phases

There is a two way coupling in terms of heat transfer between the fluid and the particle phase. The fluid to particle heat transfer is found by summing the contributions of all particles belonging to a particular Eulerian cell. The source term for the heat exchange  $S_h$  is given as follows by the Equation 2.4,

$$S_h = \frac{\sum_{\forall i \in cell} f_{cell}^i h_{fp}(T_{p,i} - T_{f,p})}{V_{cell}}, \quad (2.34)$$

where the term  $T_{f,p}$  denotes the temperature of fluid at the particle location,  $T_{p,i}$  represents the temperature of the  $i$ -th particle belonging to a cell.

### 2.4.3 Mass exchange between the phases

The spray liquid from the droplets that are deposited over the surface of the particle will get vaporized and get converted into moisture phase in the presence of heat. The rate of evaporation is dependent on the difference in concentration of the moisture content between the gas phase and the surface of the particle. The evaporation is also dependent on the surface area of the particle available for evaporation. The expression for coupling between the two phases is given as follows,

$$S_m = \frac{\sum_{\forall i \in cell} f_{cell}^i k_m A_p (w_f^* - w_f)}{V_{cell}}. \quad (2.35)$$

## 3 Methodology

This Chapter explains the different methodologies used in the project, describing parts of the implementation and discretization as provided in the IPS Fluidization software. This chapter is divided into three different sections. In the Section 3.1, a brief description of the CFD solution procedure is given, followed by Section 3.2 on DEM algorithm and finally in Section 3.3, the coupling strategies are explained.

### 3.1 CFD solution procedure

In this section, the procedure used by fluid flow solver IBOFlow<sup>©</sup> to solve for the flow variables is explained. IBOFlow is based on a unique immersed boundary technique using the finite volume method to discretize the equations on a Cartesian octree grid which can be dynamically refined and coarsened. The solver works on a segregated approach. The Navier Stoke Equations (see Equation 2.1 and Equation 2.2) are first solved using the SIMPLEC method, for more information about this method refer [50]. The temperature is solved using the Equation 2.4. The interpolation scheme by Rhie and Chow [51] is used. The implicit Euler scheme is used for time integration, as it is unconditionally stable. Finally, for the convective terms, the Ultimate quickest scheme, which is third order accurate in space, is used. Due to the immersed boundary technique no a priori meshing is required.

### 3.2 DEM algorithm

In this section, the DEM algorithm is described. A flow chart describing the general DEM algorithm is shown in Figure 3.1. There are different steps involved in the DEM algorithm. In the first step, the location and the size distribution of the particles are defined by the user. There are different possible ways of describing such an arrangement. The two ways of particle arrangement available in the solver, IPS Fluidization<sup>TM</sup>, are the cylindrical and the box arrangement. The image of two such arrangements is shown in Figure 3.2. The solver IPS Fluidization has the possibility to model particles of the same size or even have particles of different sizes.

The second step involved is to identify the collisional neighbors. This is done by sorting the list of particles based on their position in combination with a highly-efficient data structure for indexing nearest neighbours. The collisional detection in IPS Fluidization is developed to work in the massively parallel environment of the GPU (further discussed in Section 3.3.2) and allows for a linear scaling of the computational time for millions of particles. The actual algorithm of the software is not disclosed.

Next, the forces between the particles are calculated based on the soft sphere approach as explained in Section 2.2.1. In the next step, other forces such as the drag and gravity are calculated and are added to the existing forces, in addition, torque on the particles is also calculated. Using the forces that are acting on the particles, the acceleration, the velocity, angular velocity and its position are evaluated by integrating the equation on a smaller time step.

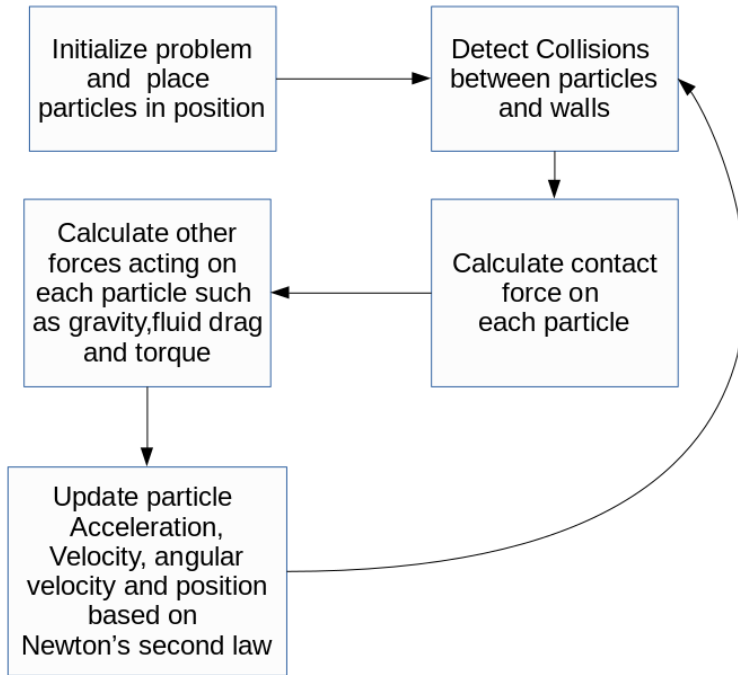


Figure 3.1: *Flowchart of the DEM Algorithm.*

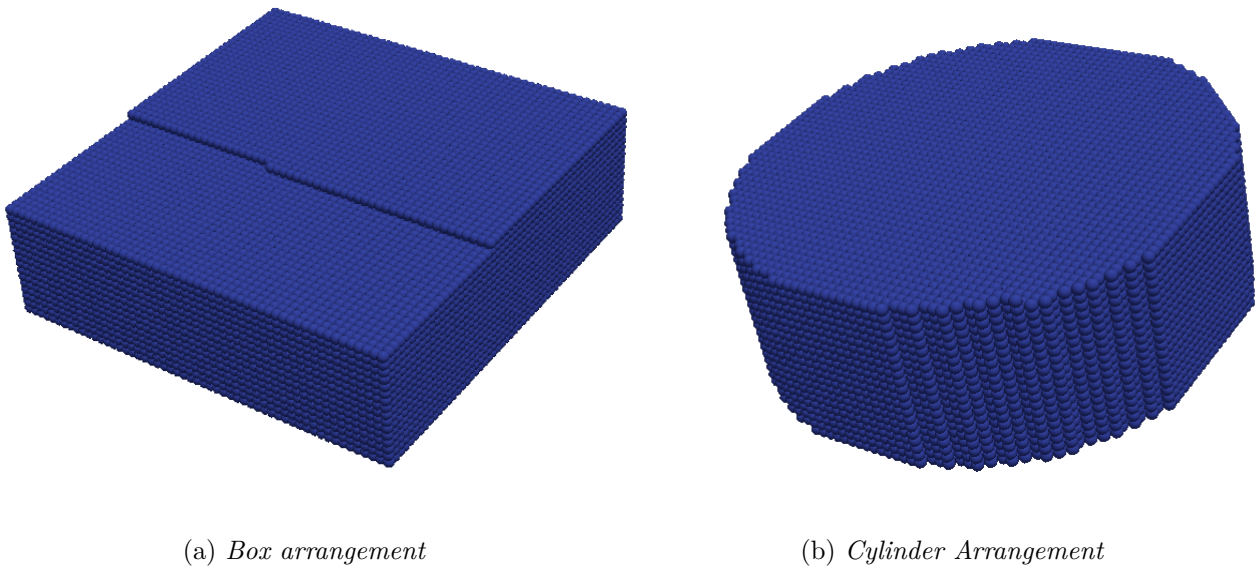


Figure 3.2: *Different Particle arrangements as available in the IPS Fluidization.*

### 3.3 Coupling method

DEM alone is computationally expensive, it is essential to accelerate the performance for the purpose of reducing the simulation time. Accelerating the performance of the simulation was previously performed in Central Processing Unit (CPU) by increasing the number of CPU cores. However, this can lead to reduced performance of coupled CFD-DEM simulations due to increase in global

communication overhead in comparison to standalone DEM and CFD simulation as shown in [52].

As an alternative, the GPU, initially developed to render images, have recently been used to perform intensive mathematical calculations for computational purposes in science and technology because of its massive parallel processing capabilities. The efficient architecture of the GPU allows one to perform multiple calculations at the same time. As an example, Radeke *et al.* [53] utilized the power of GPUs to successfully simulate millions of particles. Thus a combination of CFD running on CPU and DEM running on GPU allows us to effectively parallelize the CFD-DEM simulations.

The GPU approach is heavily used in IPS Fluidization<sup>TM</sup>, where all particle and spray computations are performed solely on the GPU.

### 3.3.1 Data transfer

There are two ways of generating a mesh in a CFD-DEM simulation. The first way is by using a single mesh for both the fluid and the particles. The other method is by using a separate mesh for both the fluid and the particles. Generally, fine grids are required to resolve the fluid flow field requirements as the accuracy of the simulation is dependent on the appropriate cell size. Decreasing the cell size can improve the accuracy of the result, however, can result in increased computational time. The main need for using fine grids is to resolve the geometrical features which influence the flow field. However, using a fine grid can affect the particle field resolution requirements. Especially in cases, where particle concentration is low inside a computational cell, as sharp changes in the solid volume fraction can happen leading to numerical instabilities. One can overcome this problem by using separate meshes for both the fluid and the particles. In this method, the particles are tracked through a coarse grid while the fluid field has a finer grid, thus, overcoming the disadvantages of using a single grid.

To efficiently transfer data between the GPU and the CPU, IPS Fluidization applies two separate grids. One grid is used for the fluid solver, for which the transport equations are discretized on the CPU, and another grid for the transfer of the information from the particles on the GPU to the fluid solver. The fluid fields such as the velocity, temperature, pressure gradient are calculated on the fluid grid and mapped to the particles in order to compute the interphase momentum and energy exchange. For the purpose of the fluid equations, the solid volume fraction,  $\epsilon_p$ , momentum  $\beta u_p$ , and energy interphase exchange terms are accumulated to the transfer grid and mapped back to the fluid grid. The complete algorithm is described schematically in Figure 3.3. To map the data from the transfer grid to the particles, the location of the center of each particle is found in an efficient manner.

In addition to that, there are two ways of calculating the volume fraction in IPS Fluidization<sup>TM</sup>. In the first method, all of the volume of the particle is accounted for in the transfer grid cell for which the particle center belongs. In the other method, the particle is split into shell sections such as exemplified in Figure 3.4. In the presented example, the particle is split 8 times in the azimuthal direction and 2 times in the polar direction and the central portion of the particle is left unsplit resulting in 33 different volumes. Each cut section has a separate center, an example is shown in Figure 3.4 a. For each particle, if the center of any of these sub-elements resides in a fluid cell, the whole volume of that sub-element is assumed to be in that cell. For example consider Figure 3.4 b, the center of cut section 15 is present in cell number 62, hence, the entire volume is assumed to be in cell number 62, in a similar way volume of section 1 is assigned to cell number 36.

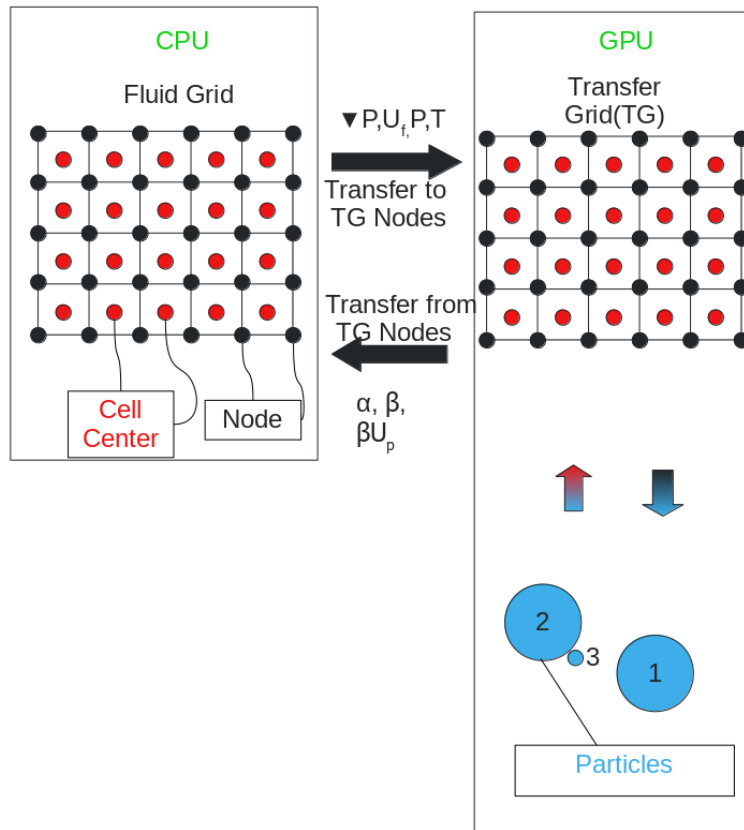


Figure 3.3: A schematic representing the data transfer mechanism between the fluid solver (CPU) and the DEM solver (GPU).

### 3.3.2 Coupling scheme

The complete coupling algorithm is shown in Figure 3.5. The fluid solver is governed by both the CPU and the GPU. The outer time step is carried out on the CPU while the inner sub iteration are carried out in the GPU. As spray process is handled in the inner sub-iterations it is also carried out on the GPU.

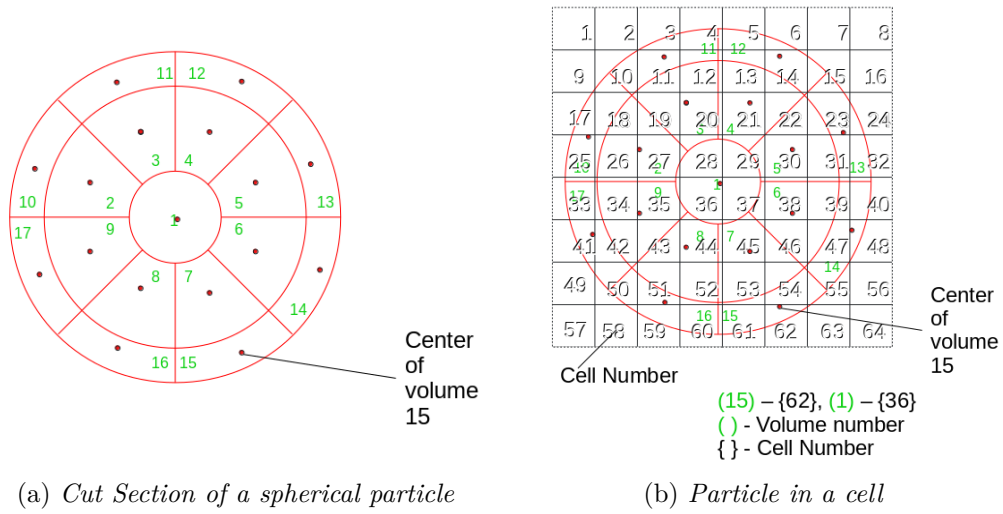


Figure 3.4: Volume fraction calculation in split method

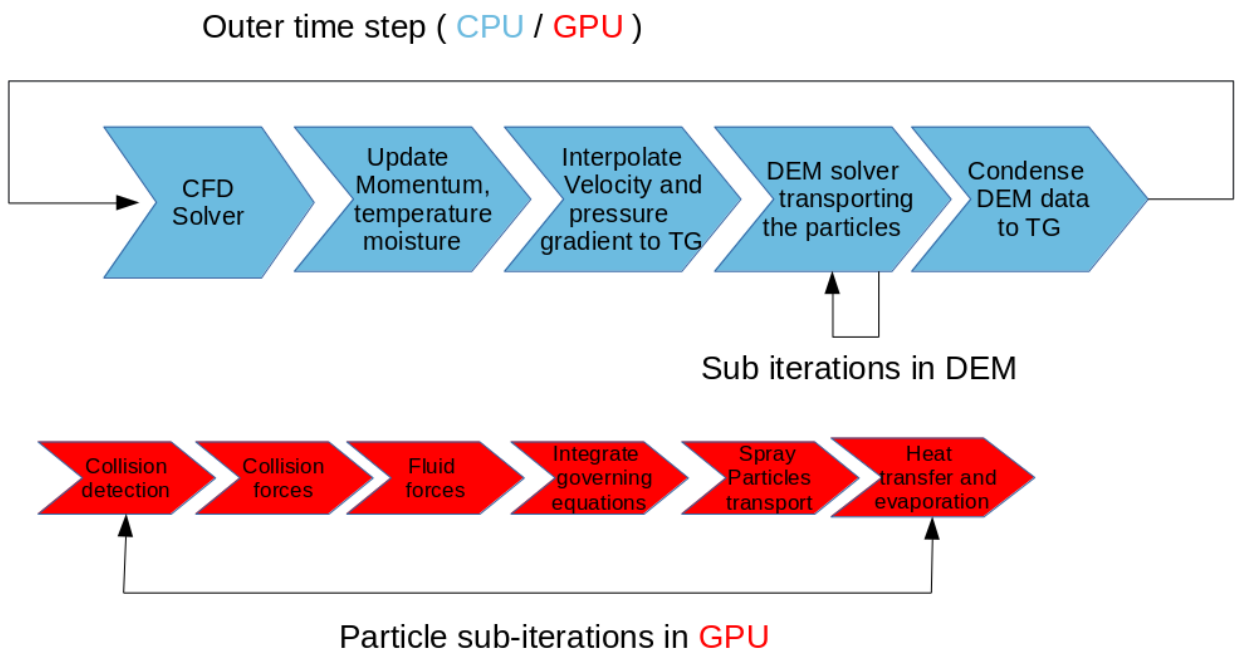


Figure 3.5: Flowchart describing the coupling Algorithm used in IPS Fluidization<sup>TM</sup>.

## 4 Simulation cases

In this Chapter, the different simulations that are performed in the project are described, giving complete details of the geometry, mesh and the solver settings. This Chapter is divided into three sections. In the Section 4.1, the settings used for performing single spout bed are described. In the Section 4.2, the description of the 1-D simulation setup that was used for performing the verification of the heat transfer model is given. Finally, in the Section 4.3, the details pertaining to the spray coating simulation are specified.

### 4.1 Single Spout Bed simulation

In order to validate the coupled CFD-DEM solver, it is essential to compare the simulation results with the experimental results. For this purpose, experimental studies conducted on a single spout bed using PEPT and PIV by Buijtenen *et al.* [14] are considered. In this section, the complete description of the geometrical setup along with the various numerical settings that are used for the simulation are described in detail.

#### 4.1.1 Geometry of the single spout bed

The simulations are carried out on a single spout fluidized bed. The schematic of which is shown in Fig 4.1. The domain comprised of a small slot in the middle of the bottom of the bed. This slot served as the spout region with a high velocity jet coming out of it. In addition to the spout region, there are inlets at the sides of the spout, these inlets served as the inlet for fluidizing air. For the purpose of reducing the computational time, the height of the domain is reduced in comparison to the experimental setup. This is deemed a valid adjustment, since the particle never reached the top of the domain in the simulations, and the bubbling region is restricted to half the size of the domain considered in the simulation. The exact dimensions of the setup that is used in the simulations are given in Table 4.1. It should be noted that the system is very shallow in the depth direction. The dimensions of the geometry are also specified in Table 4.1. A figure describing the geometry along with the dimension is shown in Figure 4.1. For the purpose of preparing the geometry for the simulations, a unit cube of side length 1 m is imported into the solver IPS Fluidization<sup>TM</sup> and scaled down to the required dimensions. The bottom region is patched and split into three regions with the spout in the middle and the other two regions serving as the inlet for the background fluidization gas.

Table 4.1: Dimensions of the single spouted bed used in the simulations.

Geometry	Length(mm)	Breath(mm)	Height(mm)
Bed	145	20	500
Spout	5	20	Nil

#### 4.1.2 Mesh and boundary conditions

An appropriate mesh size is chosen with little compromise between the accuracy and the computational time. For this purpose, the numerical simulation conducted in [14] is used as a reference. The number of cells in the length span  $N_x$  is kept as 29 with each cell having a width of 5 mm, while the number of cells for the height and the width ( $N_z$  and  $N_y$ ) are kept as 64, 2.

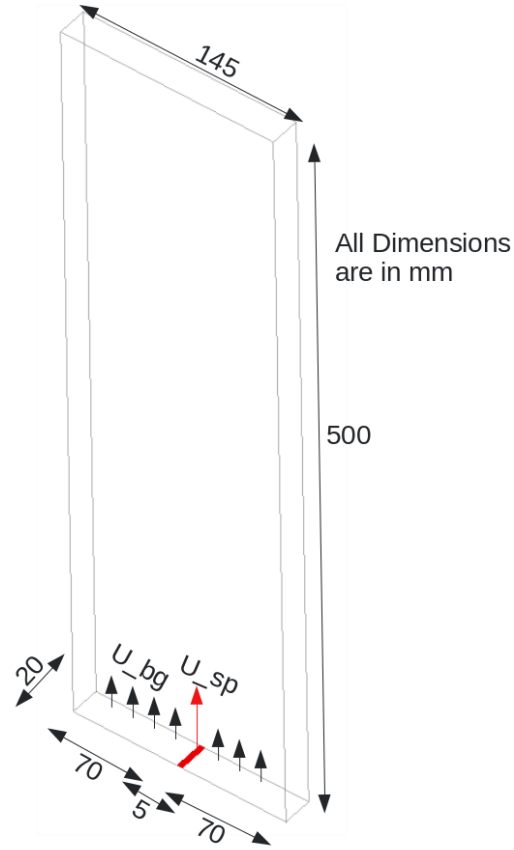


Figure 4.1: *Schematic of Single Spout bed.*

The boundary conditions used in the setup is given as follows, the simulations comprised of two inlets one for the background air and the other for the spout both being placed at the bottom of the domain, the outlet is placed at the top of the domain in the vertically opposite direction to the inlet. The spout and the background velocity are set to a value of 43.5 m/s and 2.4 m/s respectively. All the other sides are considered as no-slip walls. The simulation comprised of 12000 particles made of glass whose properties are taken from Buijtenen *et al.* [14] and is given in the Table 4.2 for reference. The size of the particles is assumed to be uniform with a diameter of 3 mm. The restitution coefficient for particle-particle collision and particle-wall collision are kept as 0.97 while the friction coefficient is kept as 0.3.

Table 4.2: Particle settings used in the simulations.

Property	Value
$d_p$	3mm
$\rho_p$	2505
$e_{n,p \rightarrow p}$	0.97
$e_{n,p \rightarrow w}$	0.97
$\mu_{fr,p \rightarrow w}$	0.3
$\mu_{fr,p \rightarrow p}$	0.3
No of Particles	12000

### 4.1.3 Physics Modelling and result extraction

The unsteady simulation on a single sprout bed is performed in IPS Fluidization<sup>TM</sup>. In the simulations, the air is used as the fluidizing medium. The properties of air are taken at ambient temperature conditions of 30°C and a pressure of 1 Bar. The temperature of the air is disregarded throughout the simulations. The effect of gravity is included in all the simulations. In the simulations three different coupling models are considered namely Koch-Hill, Beetstra, and the Ergun-Wen-Yu model. The models are verified using separate test cases before they are actually implemented to the solver. The settings that are used for the verification study are given in Section 4.1.3. The simulations are conducted for a total time of 4 s with a fluid time step of  $1 \times 10^{-4}$  s which is selected based on and a particle time step of  $1 \times 10^{-6}$  s. The particle time step is evaluated based on the criteria given by O’Sullivan and Bray [54] and is found to be  $1 \times 10^{-5}$  s, however for the simulations a lower value of  $1 \times 10^{-6}$  s is taken in order to ensure better accuracy. In order to post process the results taken from the simulations, time averaged axial velocities are measured using two line probes that are placed at a height of 0.05 m and 0.10 m from the bottom of the bed. The location of the line probes are depicted in Figure 4.2.

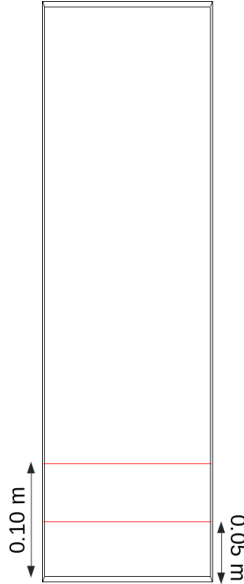


Figure 4.2: *Line probes location*

### Verification of the momentum transfer co-efficient

The verification of the different models is conducted using the numerical results of Lundberg and M Halvorsen [55]. For the purpose of verifying the models, the momentum transfer co-efficient is calculated. The momentum transfer co-efficient is a function of gas density, gas viscosity, volume fraction of gas, particle diameter and the slip velocity (difference in velocity between the fluid and the gas phase). For comparison, all of the parameters are kept constant except the slip velocity which is a function of fluid volume fraction. The properties of the parameters that are used for the verification studies are given in the Table 4.3.

Table 4.3: Properties used in calculation of momentum transfer co-efficient for the verification study.

Diameter	154 $\mu\text{m}$
Gas Density	1.225 $\text{kg}/\text{m}^3$
Gas viscosity	$1.7894 \times 10^{-5}$ $\text{kg}/\text{m}\cdot\text{s}$
Slip Velocity	$0.133/\epsilon_f$

## 4.2 Heat transfer Simulation

In this Section 4.2, settings that are deployed to perform verification studies on the heat transfer solver are described. due to lack of experimental data only verification studies are performed.

### 4.2.1 Numerical settings used for heat transfer model verification

It is essential for the heat solver to be verified as this dictates the rate of evaporation from the liquid spray present over the particle. The implementation of the heat transfer models is verified by conducting single particle simulations in IPS Fluidization<sup>TM</sup> and comparing it with results from a 1D simulations carried out using a separate 1D model. The unsteady heat transfer simulation is carried out using a single particle. In the simulations, the temperature of the particle is initiated to a value of 273 K while the temperature of background fluid is varied from 283 K to 313 K in steps of 10 K. The particle is fixed in space as the effect of gravity is neglected and the background fluid is considered stagnant. Water is used as the background fluid with all its properties taken at ambient conditions. The fluid time step is kept as  $1 \times 10^{-4}$  s while the particle time step is kept as  $1 \times 10^{-6}$  sec. The simulations are performed for a total time of 5 s. For results comparison, time evolution of the temperature from both the IPS Fluidization<sup>TM</sup> and the 1D model are compared. After which the time independence of the heat solver is verified, by extending the same simulation in IPS Fluidization<sup>TM</sup> with two more fluid steps (1e-4 s , 1e-6 s).

## 4.3 Spray Simulations

The most widely used apparatus in pharmaceutical and chemical industries for coating and drying of pellets is a Wursted fluidized bed. In order to replicate the same conditions as in the industries, the simulations are performed on the Wursted fluidized bed. For this purpose, the experimental studies conducted by Liang *et al.* [36] on a Wursted fluidized bed is considered. The geometrical details of the setup used in the simulations taken from [36] are given in the Section 4.3.1. In the subsequent Section 4.3.2, details of the mesh and the boundary conditions used in the simulations are described.

### 4.3.1 Geometry of the Wurster Bed

The main components of the Wurster bed are the Wurster column, the spray nozzle and the distributor plate. The distributor plate, which is mainly used as an input for the fluidizing air is placed at the bottom of the bed and is divided into sections. The geometry of the simulation chamber used in the simulations is given in Figure 4.3. The total height of the simulation chamber is 417 mm with the top and bottom diameters as 250 mm and 100 mm respectively. The Wurster column is placed at a height of 15 mm from the bottom of the distributor plate, the diameter of the Wurster column is 50 mm and it has a height of 60 mm. The truncated conical section of the simulation chamber has a

height of 220 mm. The spray nozzle is placed at the bottom of the bed, it has an inner and outer diameter of 12 mm and 5 mm respectively. The complete dimension of the bed is given in Table 4.4 with the cross sectional view showing the dimensions given in Figure 4.4.

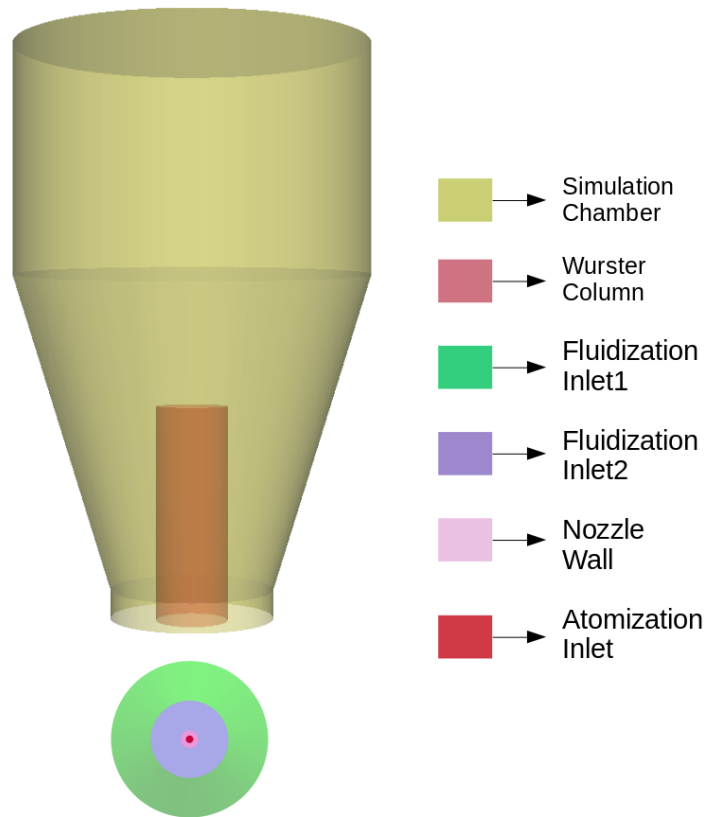


Figure 4.3: *Schematic of the Wursted bed geometry representing different boundary regions.*

Table 4.4: Wursted bed Dimensions

Variable	Value in mm
Height of the truncated cone, $H_C$	220
Height of the expansion chamber, $H_E$	160
Height of the Wurster column, $H_W$	60
Height of the gap of Wurster column, $H_P$	15
Height of the Wurster, $H_T$	417
Diameter of expansion chamber, $D_C$	250
Outer Diameter of the bottom fluidizing plate, $D_B$	100
Internal Diameter of the bottom fluidizing plate, $D_E$	52
Diameter of the Wurster column, $D_W$	50
Outer Diameter of the nozzle, $D_O$	12
Inner Diameter of nozzle, $D_I$	5

### 4.3.2 Mesh and Boundary conditions

Two different sets of simulations are carried out. The first simulation is used for validation of the Wurster case setup, while the second simulation is used for performing spray simulation on a large scale. The mesh and the boundary conditions used for these two cases are described below.

#### Case 1 : Validation simulations without heat transfer and spray

The simulations are performed without the spray and the heat transfer, on the geometry as described in the Section 4.3.1. The purpose of the simulation is for validating the setup. The number of cells in the x, y, z direction are kept as (40 X 40 X 200) respectively. In addition, the mesh is refined close to the inlets for accurately capturing the inlet velocities. There are two inlets in the domain, one served as the inlet for the atomizer and the other for the fluidizing air. The inlet boundary condition for the spray is imposed at the internal diameter of the nozzle, with a flow rate of  $3.5 \text{ m}^3/\text{hr}$ . The total mass flow rate in the distributor plate is kept constant, with a flow rate of  $73.5 \text{ m}^3/\text{hr}$ . The distributor plate had two regions, the outer annulus region which had 45 % of the total flow rate and the central region which had 55 % of the total flow rate. The size of particles is kept constant with a diameter of  $1749 \mu\text{m}$ . The number of particles are calculated corresponding to a total mass of 200 g of particles.

#### Case 2 : Large scale spray simulations

In this simulation, the effects of spray and the heat transfer are incorporated, simulations are performed in the same geometry as described in the Section 4.3.1. The same mesh as in the first case is used. In addition to the background air, the spray is introduced from the center of the atomization nozzle using a cone injector with a cone angle of  $30^\circ$ . The mass flow rate for the spray is kept as 5 g/min. The spray solution comprised of a liquid and a solid part where the mass fraction of the solid part is kept as 0.2. The diameter of the spray particles is kept as constant with a diameter of  $30 \mu\text{m}$ . As the purpose of the simulation is to model a pilot scale setup, the number of particles is significantly increased to 1.5 million. This is achieved by reducing the radius and increasing the total mass of the particles to 1400 g. The size of the particles is taken as a normal distribution with their radius varying from  $250 \mu\text{m}$  -  $500 \mu\text{m}$ . The simulation is carried out with three different spray flow rates  $2.8 \text{ m}^3/\text{hr}$ ,  $3.5 \text{ m}^3/\text{hr}$  and  $4.2 \text{ m}^3/\text{hr}$ . The temperature of the ambient air streaming out of the distributor plate is kept higher than room temperature to a value of 353K to facilitate evaporation.

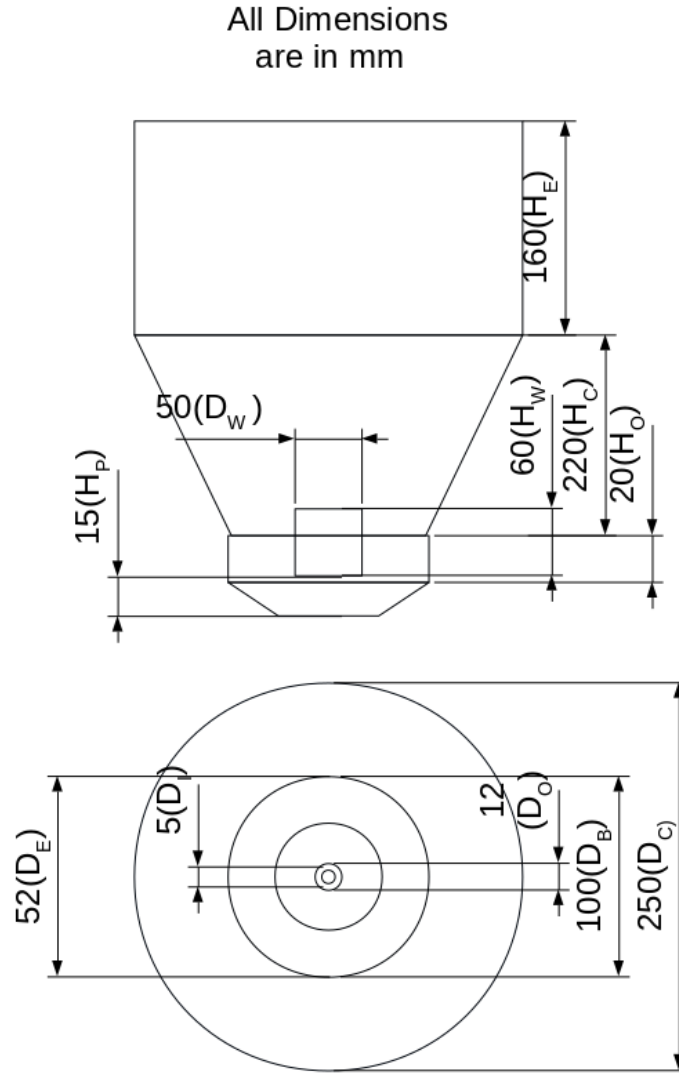


Figure 4.4: *Sectional view of the Wurster bed along with the dimension.*

### 4.3.3 Physics Modelling and result extraction

Similar to the previous Section 4.3.2, this is also categorized into two different cases. As some of the settings are common to both the cases they are just described once.

#### Case 1 : Validation simulations without heat transfer and spray

The particle properties used in this case are given in the Table 4.5. The simulation is carried for a total time of 21 s using the Ergun-Wen-Yu drag model. The model is taken so as to compare the results taken from [56] where they had used the combination of Ergun-Wen-Yu drag model. The time step for the particles and the fluid is kept as  $5e-6$  s and  $1e-4$  s respectively. The air is used as the fluidizing gas and its properties are taken at ambient conditions. The time averaged axial velocity of the particle is measured at a height of 90 mm for validation purpose.

Table 4.5: Particle settings used in the Wurster simulations.

Property	Value
$\rho_p$	2505
$e_{n,p \rightarrow p}$	0.83
$e_{n,p \rightarrow w}$	0.8
$\mu_{fr,p \rightarrow w}$	0.2
$\mu_{fr,p \rightarrow p}$	0.53

## Case 2 : Large scale spray simulations

This case included additional models for heat (see Section 2.2.2) and the spray (see Section 2.2.3). The particle properties are kept the same as of the previous case. The initial temperature of the particles and the background air is kept as 353 K to facilitate evaporation. The inlet temperature at the distributor plate is also kept as 353 K. To facilitate the transfer of moisture from the particle surface to the ambient air it is essential to give the initial condition of the moisture present in the gas phase. The properties of moisture are as given in the Table 4.6. The time step for the particles and the fluid is kept as 5e-7 s and 1e-4 s respectively. The air is used as the fluidizing gas and its properties are taken at ambient conditions. The simulations are carried out for a total time of 5 sec. The results are taken in the form of histogram, in order to establish the correlation between the coating thickness and the radius. Also, to study the effect of flow rates on the thickness of the coated film.

Table 4.6: Moisture Properties used in the spray simulations.

Moisture Properties	Value	Unit
Viscosity	9.4e-6	kg/m.s
Density	0.294	kg/m <sup>3</sup>
Thermal conductivity	0.0193	W/mK
Molar mass	18.01528	kg/kmol
Diffusion coefficient	2.8e-5	m <sup>2</sup> /s
Boiling point	373	K
Enthalpy of evaporation	2260	kJ/kg

## 5 Results and Discussion

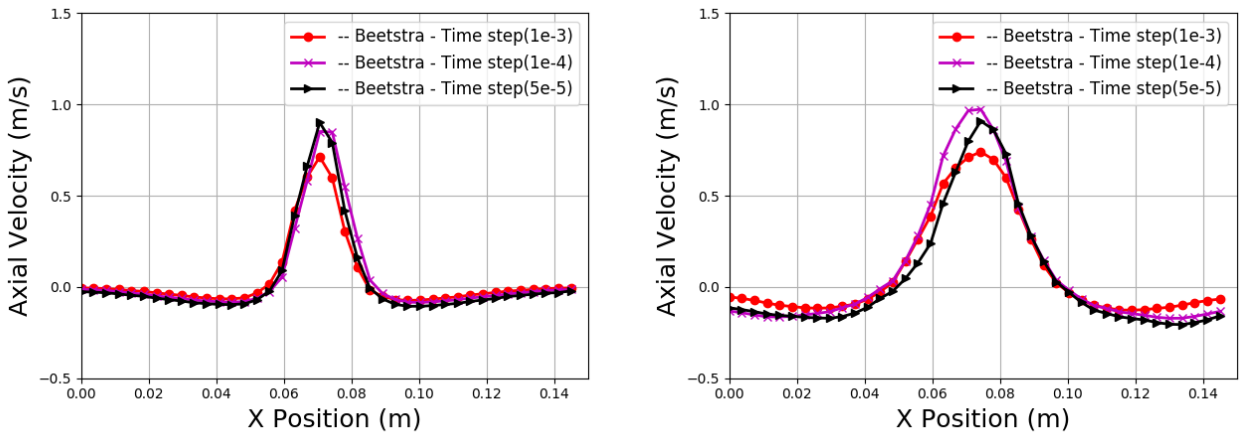
In this chapter, the results obtained from the different simulations, as described in Section 4, are presented and discussed. This chapter comprises of three sections. In the Section 5.1, the results obtained from the single spout simulations are shown and some important parameters are studied. In the Section 5.2, the results retrieved from 1D heat transfer simulations are discussed. Finally, in the Section 5.3 the results of the spray simulations are presented.

### 5.1 Single spout bed simulations

This section illustrates the results that are obtained from the single spout bed simulations. The simulations in this section, are performed for validating and testing the performance of IPS Fluidization<sup>TM</sup> solver. The results are obtained using the procedure as explained in the Section 4.1.3. Furthermore, systematic studies are performed, to study the effect of various parameters influencing the flow behaviour in a coupled setup.

#### 5.1.1 Effect of fluid time step

The fluid time step used in the simulations plays a crucial role in the coupling accuracy and also on the total simulation time. In order to achieve a time independent solution, it is essential to select an appropriate time step. For this purpose, fluid time step was varied until a time independent solution was obtained. The Figure 5.1, shows the results of time averaged axial velocity obtained from the simulation using various fluid time steps. The results obtained at heights (0.05m and 0.10m) are shown in Figures 5.1a and 5.1b respectively. In both the plots, good agreement in the results is observed when the fluid time step is less than  $1 \times 10^{-4}$  s. Hence, it can be concluded that the solution is time independent after  $1 \times 10^{-4}$  s and thus, will be taken for further simulations.



(a) Velocity at a height of 0.05m

(b) Velocity at a height of 0.10m

Figure 5.1: Comparison of time averaged axial particle velocity for different fluid time steps.

### 5.1.2 Momentum-Models

In this section, the three different momentum exchange models, as given in Section 2.4.1 are compared. The models are verified using 1D models before they are tested in the solver using actual 2D spout simulations. This section is further split into two section. In the first subsection, the results obtained from the verification studies for comparing momentum transfer coefficient is presented followed by the validations studies in the subsequent section.

#### Verification of the Momentum transfer coefficient

The momentum transfer coefficient is calculated by varying the particle volume fraction. The Figure 5.2, shows the comparison between the 1D models and the numerical results given in the literature [55]. It is found that the momentum exchange coefficient increases with increasing particle volume fraction. The 1D results obtained from the Koch-Hill model tends to under predict the values in comparison to numerical results from literature when the particle volume fraction is less than 0.4. Also, Koch-Hill model is found to give higher value of momentum exchange coefficient, at higher particle volume fraction in comparison to Gidaspow model. Good agreement is observed, in case of Gidaspow model. However, Beetstra model couldn't be verified due to unavailability of results in the literature. All three models are further studied using 2D single spout simulations. The results of which are discussed in subsequent section.

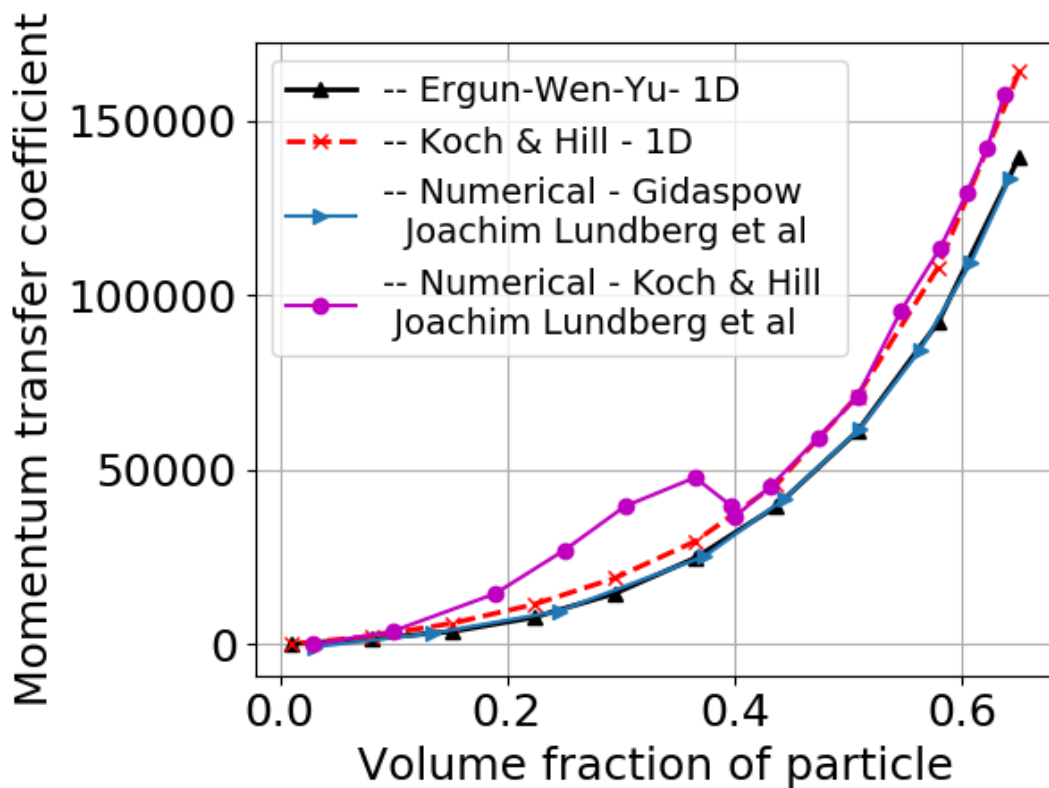
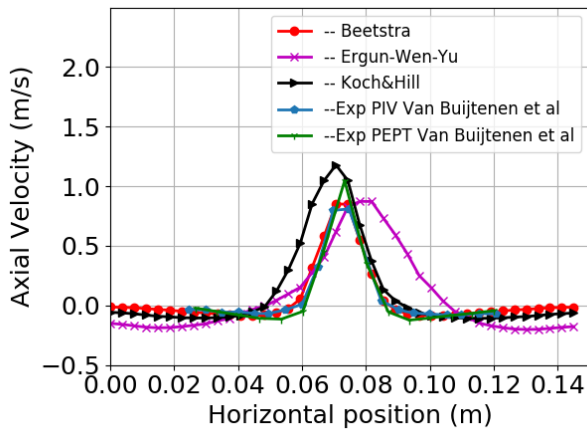


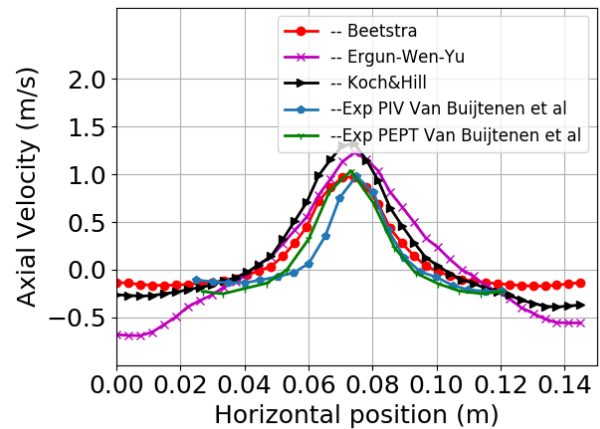
Figure 5.2: Comparison of Momentum transfer coefficients

## Comparison of drag models using 2D single spout simulations

The simulations are conducted with the same geometry as described in Section 4.1.1 and the time step is selected based on the results from the Section 5.1.1. The result obtained is shown in Figure 5.3. It can be seen, that the beestra model has a close agreement with the experimental results of PIV, while Ergun-Wen-Yu and Koch-Hill model tends to over predict the values. The behaviour of the models are found to be different at different region of the bed. The main regions of interest are the spouting region where the drag is dominant and the annulus region (close to the wall). In the spout region, Ergun-Wen-Yu model has the highest value of velocity, while the Beestra model has the lowest value. Outside the spout region, the trend is reversed as expected. This is because, in the spouting region the particles receive a higher momentum and as a result there is a much more pronounced re-circulation which results in a higher velocity magnitude in the Koch-Hill and Ergun-Wen-Yu models. The vector plot for the same is given in Figure 5.4. The figures from left to right represent Ergun-Wen-Yu, Koch-Hill and Beestra models respectively. The two red lines denote the location of the probe used of measurement respectively. It can be clearly inferred from the figure that, there is higher re-circulation closer to the walls, in case of, Ergun-Wen-Yu and Koch-Hill model. Also, the magnitude of re-circulation is higher in one side compared to other in these models. This skewness cause the stream to shift direction towards the side with higher re-circulation. The average velocity of the particle increases higher in domain, as more particles come in contact with the high velocity fluid stream. As a result. the width of the curve widens as seen in Figure 5.3b.



(a) Velocity at 0.05m



(b) velocity at 0.10m

Figure 5.3: Time averaged particle velocity for different momentum exchange models.

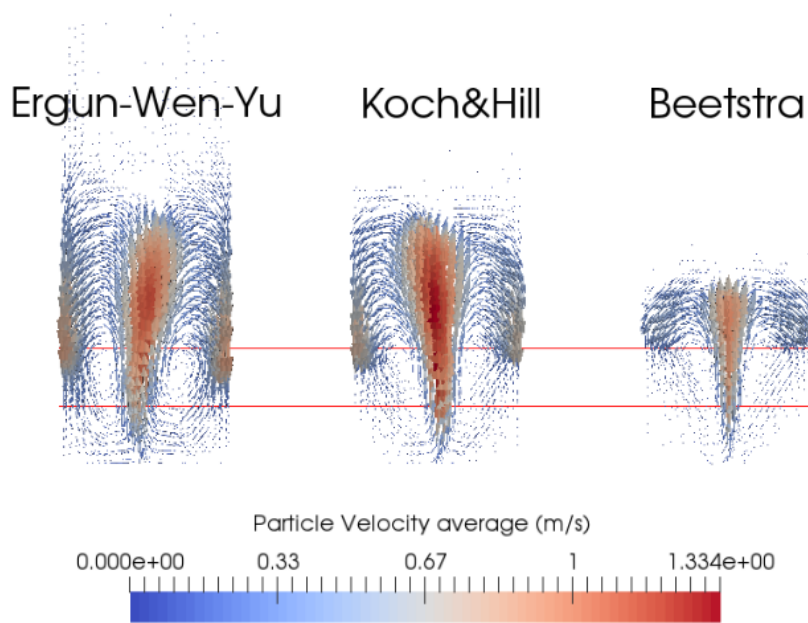


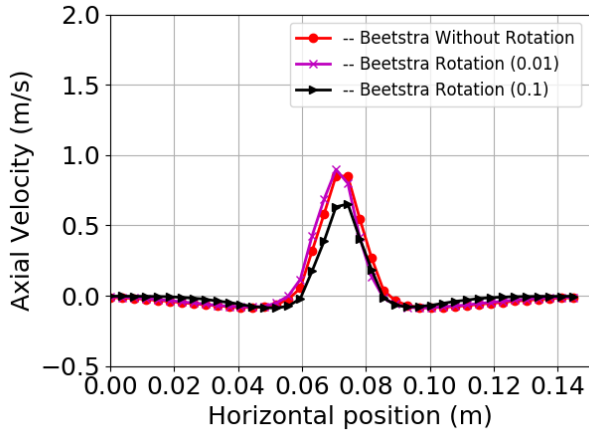
Figure 5.4: *Vector plot of time averaged particle axial velocity plots for three different momentum-exchange models at the end of the simulation (4 sec).*

### 5.1.3 Effect of rolling friction

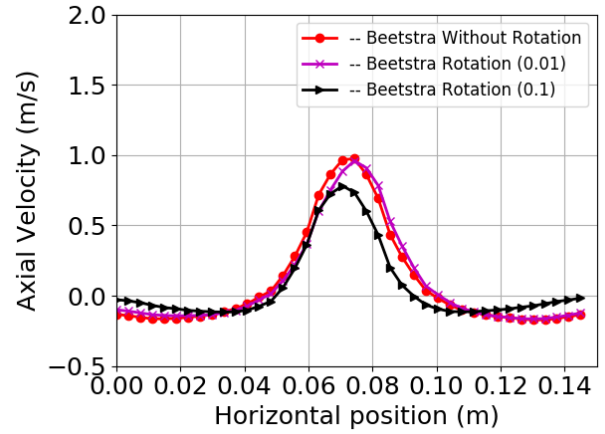
The effect of change in rolling friction of the particles, on the flow characteristics is evaluated. Three different values of rolling friction coefficient (0, 0.01, 0.1) are compared in the simulations. The results are shown in Figure 5.5. In the region closer to the spout, the velocity profile is same for cases with lower values of rolling friction. This is because in the spout region, the drag force is the dominant force, as a result, the number of inter-particle interactions are lower. However, as rolling friction increases, there is more pronounced energy dissipation during inter particle collisions resulting in significantly lower velocity. In the near wall region, the velocity profile varies as rolling friction changes. This is because, there are more inter particle collisions leading to lower axial velocities magnitude owing to higher loss of energy.

### 5.1.4 Effect of friction

The effect of friction coefficient of the particles is analyzed for three different values (0.3, 0.5, 0.7). The results obtained are presented in Figure 5.6. A similar trend as in case of rolling friction was observed. In the wall region, the magnitude of particle velocity decreases as friction coefficient increases due to increased energy dissipation at higher friction coefficient. In the spout region, there is very little difference in the curves. Thus, it can be clearly seen that, rolling friction is more dominant in the spout region in comparison to static friction as particles are always in motion in this region.

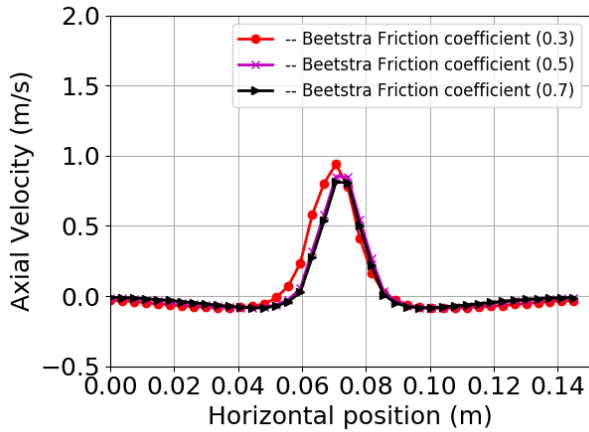


(a) Velocity at 0.05m

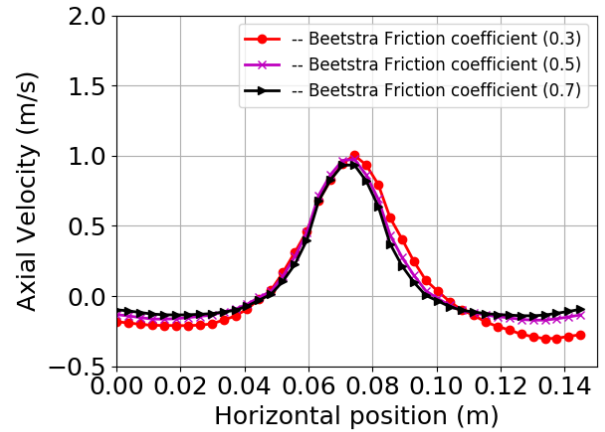


(b) velocity at 0.10m

Figure 5.5: Time averaged particle velocity for different values of rolling friction



(a) Velocity at 0.05m



(b) velocity at 0.10m

Figure 5.6: Time averaged particle velocity for different friction-coefficient

## 5.2 1D heat transfer simulations

In this section, the result obtained from the heat transfer simulations carried out using IPS fluidization<sup>TM</sup> and the 1D model are presented. In Figure 5.7, time evolution of temperature are compared. In all the cases, the temperature of the particle increases until it reaches the stagnant air conditions. Good agreement in the results are observed with the 1D simulation which verifies the implementation of the heat transfer model. In addition to verifying the heat transfer model in the solver IPS fluidization<sup>TM</sup>, the fluid time step is also varied to check the accuracy of the solver. The results can be seen in Figure 5.8. Although, all three time step gives the same time evolution of temperature, this may not give an exact representation of the time step that is required to obtain a time independent solution as the background air is considered stagnant in the current simulation. However, it verifies that the solver is stable even for longer time steps in simple cases. The validation of the heat transfer cannot be performed due to difficulty in finding an ideal data from the literature.

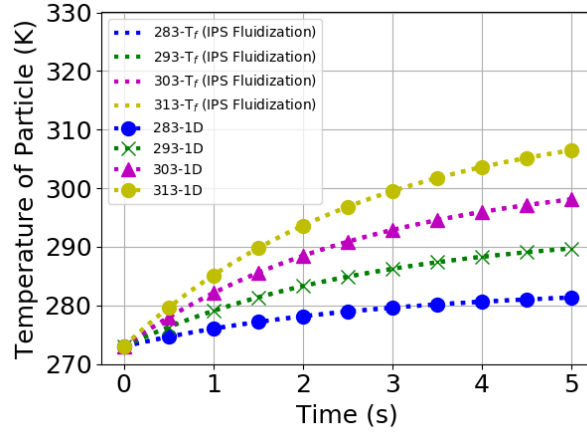


Figure 5.7: Comparison of time evolution of temperature between the 1D simulation and IPSFluidization.

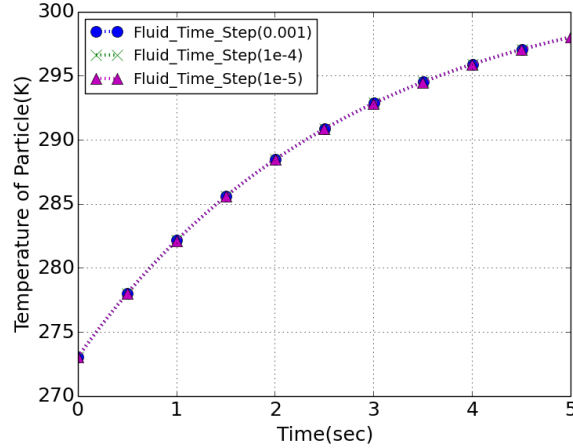


Figure 5.8: Comparison of time evolution of temperature for different fluid time steps.

## 5.3 Spray simulations

This section represents the results obtained from the spray simulation. This section is categorized into two subsections, in the first section, the case setup used in the simulation is validated against experiment results obtained from [36]. In the subsequent section, the results obtained from the spray simulations are presented.

### 5.3.1 Wurster bed simulations

The Figure 5.9 shows the comparison between the experimental values used in [36] and the Wurster bed simulation carried out in IPS Fluidization<sup>TM</sup>. Since the domain is axisymmetric the results are obtained along a radial line. The average axial velocity of the particles is plotted against the radius of the domain, with zero being the center and the maximum being the wall. Good agreement in the results are observed in the spout region, while the velocity is slightly over predicted in the region closer to the walls. This error might be caused by a difference in values of rolling friction and friction coefficient used in simulations compared to the particle properties used in the experimental setup.

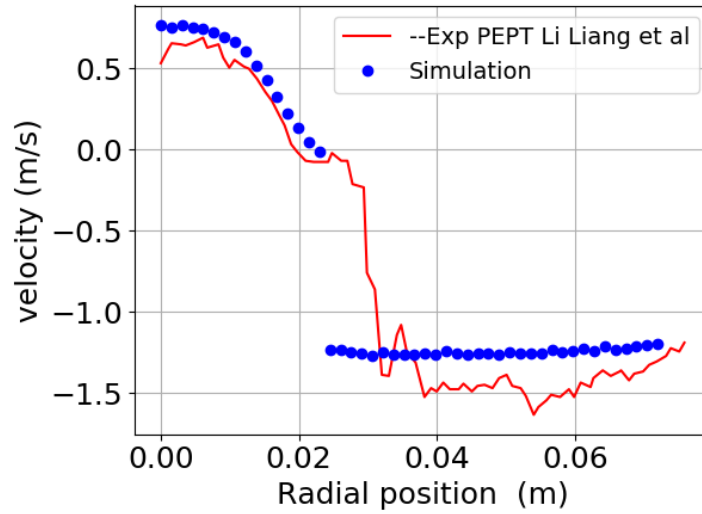


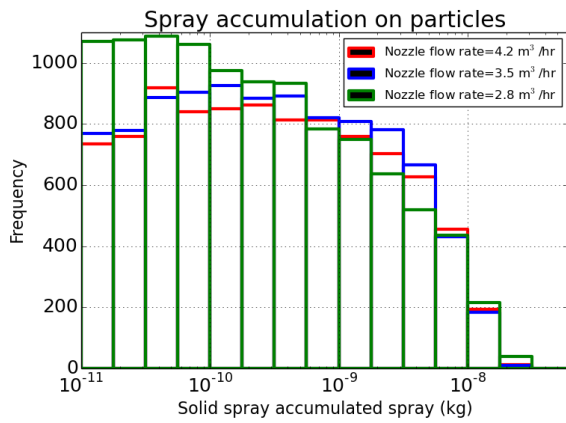
Figure 5.9: Comparison of axial velocity from simulation with the experimental study of Li Liang et al.

### 5.3.2 Wurster bed spray simulations

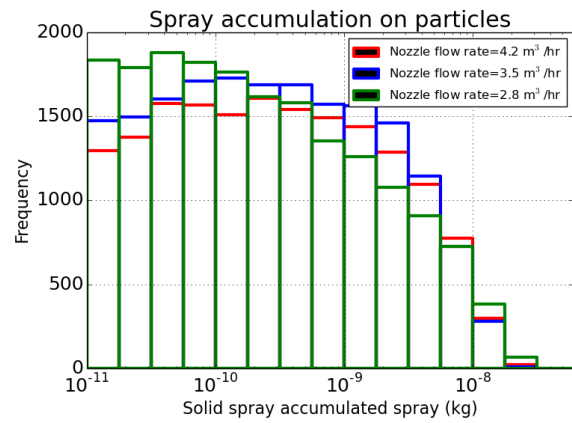
In this section, the results obtained from spray simulations are presented. Figure 5.10 shows the histogram plot of particles with a given coating thickness for various nozzle flow rates. As observed from Figure 5.10a - 5.10d, the number of particles with a coating thickness, increases significantly as time progresses. This is because more particles come in contact with the spray over time. This is clearly shown in Figure 5.11, where the time evolution of the accumulated mass is shown for a single case. The number of particles having thinner coating is higher for higher flow rates. This is because at higher flow rates, more particles come in contact with spray. However, at higher flow rates, the particles are exposed to larger drag force and hence, they are faster transported from the spray injection zone.

### 5.3.3 Correlation between particle radius and thickness of the film

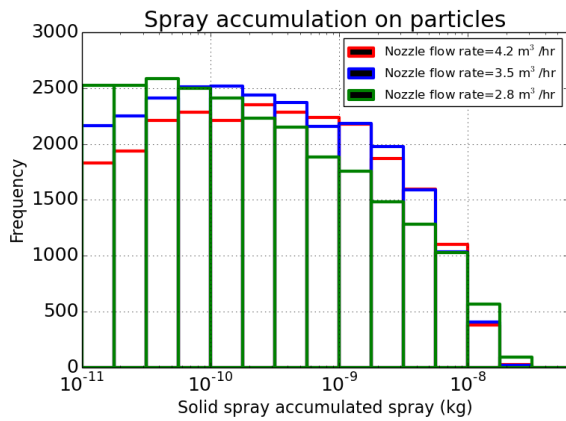
In order to study the correlation between the particle radius and the thickness of the coating, marginal plots are plotted. A marginal plot allows to study the relationship between two numeric variables. The marginal charts, at the top and at the right, shows the distribution of the two variables using the density plots, while the central chart displays their correlation. In the Figure 5.12, the correlation between particle radius and thickness of deposited film is plotted. The plot at the top, shows the distribution of particles with a given radius having coating, i.e. that has been hit by at least one spray droplet. While the plot on the right side, displays the distribution of accumulated droplet mass, independent of the radius. In the center, the correlation plot is shown. A total of 43992 particles have been hit by the spray out of 1.4M particles after a time of 5s. The density plot at the top and right shows only the particles that has been hit by the spray. From the top, density plot, it can be inferred that, there are more number of bigger particles having coating in comparison to smaller particles. This is because bigger particles have higher surface area and hence probability of them have collision with spray parcels is higher. Also bigger particles have higher mass and stay close to the spray region due to reduced drag per mass, thus creating a shielding effecting for smaller particles. From the right, density plot, it can be seen that, there are more of particles having thinner film in comparison to



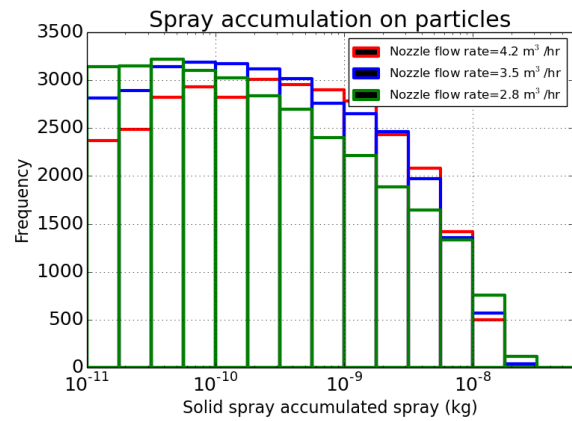
(a) After 2 sec of spray



(b) After 3 sec of spray



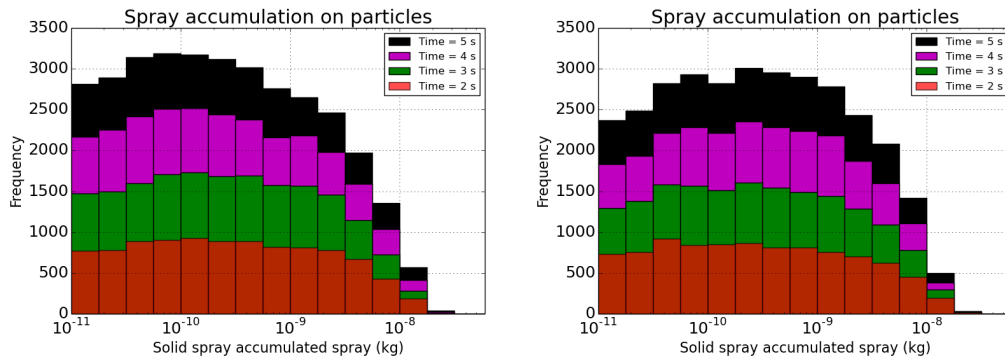
(c) After 4 sec of spray



(d) After 5 sec of spray

Figure 5.10: Histogram plot showing spray accumulation over the particles at different time intervals for various flow rates.

thicker film. For the central plot, the darker the region, better the correlation, for example, if we take a particular value of solid spray mass from y axis, and move along positive direction of x axis, the number of particles having that thickness increases for bigger particles. Similarly, if we take a particular radius on the x axis, and move along the positive direction of y axis, there are more number of particles with less mass accumulated in comparison to more mass accumulated.



(a) Spray accumulated for flow rate  $3.5 \text{ m}^3/\text{hr}$  (b) Spray accumulated for flow rate  $4.2 \text{ m}^3/\text{hr}$

Figure 5.11: Spray accumulation over time with varying flow rates

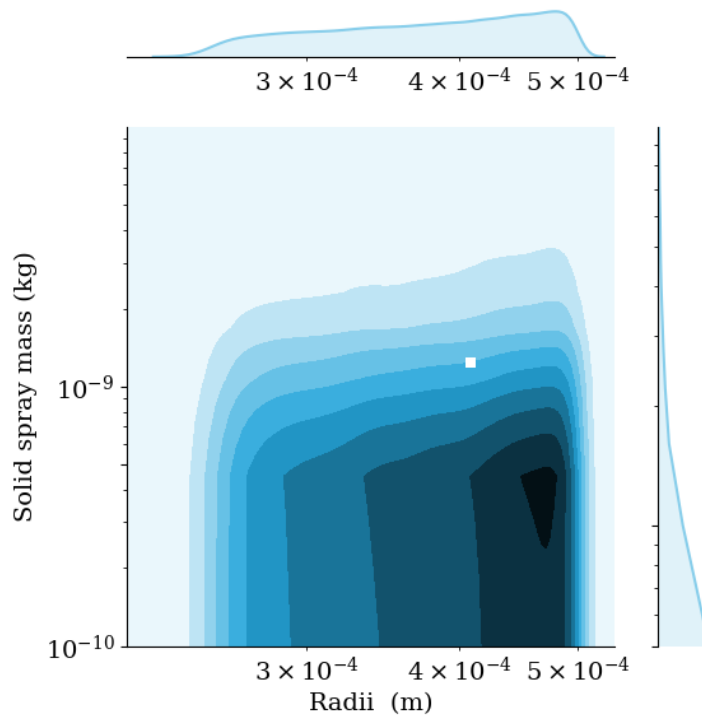


Figure 5.12: Plot showing correlation between the radii of the particle and the spray accumulated for Nozzle Flow rate =  $4.2 \text{ m}^3/\text{hr}$

## 6 Conclusion

The main objective of this thesis has been to simulate and study the pellet coating process, as well as, to test the scalability of the solver in carrying out computational intensive simulations with more than a million particles with the spray treated in a Lagrangian manner.

The study was carried out in three parts, in the initial phase, the single spout simulations were carried out using the solver IPS Fluidization<sup>TM</sup> developed at FCC with an aim to validate the coupled solver. The solver was found to be time independent after a fluid time step of 0.1 ms for such simulations. Three different momentum exchange models were compared against experimental data available in the open literature. The Beetstra momentum model, was found to produce accurate results and showed close agreement with the PIV experimental results from [14]. Further, the effect of rolling friction and friction coefficient of particle were evaluated. It was found that, as rolling friction was increased, the loss of energy during each interparticle collisions was also significantly higher, resulting in reduced velocity magnitude.

The heat transfer model, which was added to the solver (IPS Fluidization<sup>TM</sup>) by FCC was verified in this thesis by using 1D models. The simulations conducted using the solver showed identical match with the 1D models and thus verifying the heat transfer model in the solver.

In order to carry out spray simulations, the setup used in [36] was used. The results were obtained in the form of time averaged axial velocity thus validating the setup. The plots showed good correspondence with the numerical values available in the literature. The number of particles in the spray simulations was scaled to be more than a million. The results were taken in the form of histogram. The general trend showed, as expected, that at lower nozzle flow rates, there were more number of particles having a thicker coating. While, at higher flow rates, there were more number of particles having a thinner coating. The results also showed that there were higher numbers of larger particles having coating in comparison to smaller particles. This is because the bigger particles have higher surface area and also they tend to stay closer to the nozzle region due to their higher mass and hence create a shielding effect for the smaller particles. The results also proved the effectiveness of the solver IPS Fluidization<sup>TM</sup> in carrying out full physics large scale coating simulations.

## References

- [1] G. L. Matheson, W. Herbst, and P. Hol, *Ind. Eng. Chem.* 1949, p. 1099.
- [2] K. B. Mathur and P. E. Gishler, A study of the application of the spouted bed technique to wheat drying, *Journal of Applied Chemistry* **5**, no. 11 1955, 624–636, 1955. DOI: 10.1002/jctb.5010051106. eprint: <https://onlinelibrary.wiley.com/doi/pdf/10.1002/jctb.5010051106>. [Online]. Available: <https://onlinelibrary.wiley.com/doi/abs/10.1002/jctb.5010051106>.
- [3] V. S. Sutkar, N. G. Deen, and J. Kuipers, Spout fluidized beds: Recent advances in experimental and numerical studies, *Chemical Engineering Science* **86** 2013, 124–136, 2013, 5th International Granulation Workshop, ISSN: 0009-2509. DOI: <https://doi.org/10.1016/j.ces.2012.06.022>. [Online]. Available: <http://www.sciencedirect.com/science/article/pii/S0009250912003715>.
- [4] A. Nagarkatti and A. Chatterjee, Pressure and flow characteristics of a gas phase spout-fluid bed and the minimum spout-fluid condition, *The Canadian Journal of Chemical Engineering* **52**, no. 2 1974, 185–195, 1974. DOI: 10.1002/cjce.5450520209. eprint: <https://onlinelibrary.wiley.com/doi/pdf/10.1002/cjce.5450520209>. [Online]. Available: <https://onlinelibrary.wiley.com/doi/abs/10.1002/cjce.5450520209>.
- [5] Chatterjee and Asok, Spout-fluid bed technique, *Industrial & Engineering Chemistry Process Design and Development* **9**, no. 2 1970, 340–341, 1970. DOI: 10.1021/i260034a032. eprint: <https://doi.org/10.1021/i260034a032>. [Online]. Available: <https://doi.org/10.1021/i260034a032>.
- [6] M. L. Passos, A. S. Mujumdar, G. Vijaya, and V. G. Raghavan, Spouted and spout-fluidized beds for gram drying, *Drying Technology* **7**, no. 4 1989, 663–696, 1989. DOI: 10.1080/07373938908916621. eprint: <https://doi.org/10.1080/07373938908916621>. [Online]. Available: <https://doi.org/10.1080/07373938908916621>.
- [7] *Spouted and Spout-Fluid Beds: Fundamentals and Applications*. Cambridge University Press, 2010. DOI: 10.1017/CB09780511777936.
- [8] W. de Oliveira, J. Freire, and J. Coury, Analysis of particle coating by spouted bed process, *International Journal of Pharmaceutics* **158**, no. 1 1997, 1–9, 1997, ISSN: 0378-5173. DOI: [https://doi.org/10.1016/S0378-5173\(97\)00181-6](https://doi.org/10.1016/S0378-5173(97)00181-6). [Online]. Available: <http://www.sciencedirect.com/science/article/pii/S0378517397001816>.
- [9] R. Cunha, K. G. Maialle, and F. Menegalli, Evaluation of the drying process in spouted bed and spout fluidized bed of xanthan gum: Focus on product quality, *Powder Technology* **107** Feb. 2000, 234–242, Feb. 2000. DOI: 10.1016/S0032-5910(99)00197-7.
- [10] W. Ludwig, R. Szafran, A. Kmiec, and J. Dziak, Dry powder coating in a modified wurster apparatus, *Procedia Engineering* **42** 2012, 437–446, 2012, CHISA 2012, ISSN: 1877-7058. DOI: <https://doi.org/10.1016/j.proeng.2012.07.435>. [Online]. Available: <http://www.sciencedirect.com/science/article/pii/S1877705812028354>.
- [11] J. Pritchett, T. Blake, and S. Garg, A numerical model of gas fluidized beds, *AIChE Symp Ser* **74** Jan. 1978, 134–148, Jan. 1978.
- [12] Y. Tsuji, T. Kawaguchi, and T. Tanaka, Discrete particle simulation of two-dimensional fluidized bed, *Powder Technology* **77**, no. 1 1993, 79–87, 1993, ISSN: 0032-5910. DOI: [https://doi.org/10.1016/0032-5910\(93\)85010-7](https://doi.org/10.1016/0032-5910(93)85010-7). [Online]. Available: <http://www.sciencedirect.com/science/article/pii/0032591093850107>.
- [13] P. Cundall and O. Strack, A discrete numerical model for granular assemblies, *English (US), Geotechnique* **29**, no. 1 Mar. 1979, 47–65, Mar. 1979, ISSN: 0016-8505. DOI: 10.1680/geot.1979.29.1.47.

- [14] M. S. van Buijtenen, W.-J. van Dijk, N. G. Deen, J. Kuipers, T. Leadbeater, and D. Parker, Numerical and experimental study on multiple-spout fluidized beds, *Chemical Engineering Science* **66**, no. 11 2011, 2368–2376, 2011, ISSN: 0009-2509. DOI: <https://doi.org/10.1016/j.ces.2011.02.055>. [Online]. Available: <http://www.sciencedirect.com/science/article/pii/S0009250911001564>.
- [15] R. Chopra, G. Alderborn, J. M. Newton, and F. Podczeczek, The influence of film coating on pellet properties, *Pharmaceutical Development and Technology* **7**, no. 1 2002, 59–68, 2002. DOI: 10.1081/PDT-120002231. eprint: <https://doi.org/10.1081/PDT-120002231>. [Online]. Available: <https://doi.org/10.1081/PDT-120002231>.
- [16] K. Jono, H. Ichikawa, M. Miyamoto, and Y. Fukumori, A review of particulate design for pharmaceutical powders and their production by spouted bed coating, *Powder Technology* **113**, no. 3 2000, 269–277, 2000, Neptis Symposium on Fluidization- Present and Future, ISSN: 0032-5910. DOI: [https://doi.org/10.1016/S0032-5910\(00\)00310-7](https://doi.org/10.1016/S0032-5910(00)00310-7). [Online]. Available: <http://www.sciencedirect.com/science/article/pii/S0032591000003107>.
- [17] A. V. Patil, E. Peters, T. Kolkman, and J. Kuipers, Modeling bubble heat transfer in gas solid fluidized beds using dem, *Chemical Engineering Science* **105** 2014, 121–131, 2014, ISSN: 0009-2509. DOI: <https://doi.org/10.1016/j.ces.2013.11.001>. [Online]. Available: <http://www.sciencedirect.com/science/article/pii/S0009250913007306>.
- [18] A. Patil, E. Peters, and J. Kuipers, Computational study of particle temperature in a bubbling spout fluidized bed with hot gas injection, *Powder Technology* **284** 2015, 475–485, 2015, ISSN: 0032-5910. DOI: <https://doi.org/10.1016/j.powtec.2015.07.014>. [Online]. Available: <http://www.sciencedirect.com/science/article/pii/S003259101500546X>.
- [19] T. Tsory, N. Ben-Jacob, T. Brosh, and A. Levy, Thermal dem-cfd modeling and simulation of heat transfer through packed bed, *Powder Technology* **244** 2013, 52–60, 2013, ISSN: 0032-5910. DOI: <https://doi.org/10.1016/j.powtec.2013.04.013>. [Online]. Available: <http://www.sciencedirect.com/science/article/pii/S0032591013002702>.
- [20] H. Wu, N. Gui, X. Yang, J. Tu, and S. Jiang, Numerical simulation of heat transfer in packed pebble beds: Cfd-dem coupled with particle thermal radiation, *International Journal of Heat and Mass Transfer* **110** 2017, 393–405, 2017, ISSN: 0017-9310. DOI: <https://doi.org/10.1016/j.ijheatmasstransfer.2017.03.035>. [Online]. Available: <http://www.sciencedirect.com/science/article/pii/S0017931016331386>.
- [21] M. Askarishahi, M.-S. Salehi, and S. Radl, Full-physics simulations of spray-particle interaction in a bubbling fluidized bed, *AIChE Journal* **63**, no. 7 2017, 2569–2587, 2017. DOI: 10.1002/aic.15616. eprint: <https://onlinelibrary.wiley.com/doi/pdf/10.1002/aic.15616>. [Online]. Available: <https://onlinelibrary.wiley.com/doi/abs/10.1002/aic.15616>.
- [22] V. S. Sutkar, N. G. Deen, A. V. Patil, V. Salikov, S. Antonyuk, S. Heinrich, and J. Kuipers, Cfd dem model for coupled heat and mass transfer in a spout fluidized bed with liquid injection, *Chemical Engineering Journal* **288** 2016, 185–197, 2016, ISSN: 1385-8947. DOI: <https://doi.org/10.1016/j.cej.2015.11.044>. [Online]. Available: <http://www.sciencedirect.com/science/article/pii/S1385894715015879>.
- [23] W. I. Kariuki, B. Freireich, R. M. Smith, M. Rhodes, and K. P. Hapgood, Distribution nucleation: Quantifying liquid distribution on the particle surface using the dimensionless particle coating number, *Chemical Engineering Science* **92** 2013, 134–145, 2013, ISSN: 0009-2509. DOI: <https://doi.org/10.1016/j.ces.2013.01.010>. [Online]. Available: <http://www.sciencedirect.com/science/article/pii/S0009250913000134>.
- [24] A. Mark and B. van Wachem, Derivation and validation of a novel implicit second-order accurate immersed boundary method, *Journal of Computational Physics* **227**, no. 13 2008, 6660–6680, 2008.

- [25] A. Mark, R. Rundqvist, and F. Edelvik, Comparison between different immersed boundary conditions for simulation of complex fluid flows, *Journal of Fluid Dynamics & Materials Processing* **7**, no. 3 2011, 241–258, 2011.
- [26] A. Mark, E. Svenning, R. Rundqvist, *et al.*, Microstructure simulation of early paper forming using immersed boundary methods, *Tappi Journal* **10**, no. 11 2011, 23–30, 2011.
- [27] T. Johnson, P. Røyttä, A. Mark, and F. Edelvik, Simulation of the spherical orientation probability distribution of paper fibers in an entire suspension using immersed boundary methods, *Journal of Non-Newtonian Fluid Mechanics*, no. 1 2016, 2016.
- [28] A. Mark, B. Andersson, S. Tafuri, K. Engström, H. Söröd, F. Edelvik, and J. Carlson, Simulation of electrostatic rotary bell spray painting in automotive paint shops, *Atomization and Sprays* **23**, no. 1 2013, 25–45, 2013.
- [29] F. Edelvik, A. Mark, N. Karlsson, T. Johnson, and J. S. Carlson, “Math-based algorithms and software for virtual product realization implemented in automotive paint shops”, *Math for the Digital factory*. Springer Verlag, 2017, pp. 231–251.
- [30] A. Mark, R. Bohlin, D. Segerdahl, F. Edelvik, and J. Carlson, Optimisation of robotised sealing stations in paint shops by process simulation and automatic path planning, *International Journal of Manufacturing Research* **9**, no. 1 2014, 4–26, 2014.
- [31] S. Ingelsten, A. Mark, and F. Edelvik, A lagrangian-eulerian framework for simulation of transient viscoelastic fluid flow, *Journal of Non-Newtonian Fluid Mechanics* **266** 2019, 20–32, 2019, ISSN: 0377-0257. DOI: <https://doi.org/10.1016/j.jnnfm.2019.02.005>. [Online]. Available: <http://www.sciencedirect.com/science/article/pii/S037702571830137X>.
- [32] J. Göhl, K. Markstedt, A. Mark, K. Håkansson, P. Gatenholm, and F. Edelvik, Simulations of 3d bioprinting: Predicting bioprintability of nanofibrillar inks, *Biofabrication* **10**, no. 3 2018, 034105, 2018. DOI: 10.1088/1758-5090/aac872.
- [33] J. Göhl, A. Mark, S. Sasic, and F. Edelvik, An immersed boundary based dynamic contact angle framework for handling complex surfaces of mixed wettabilities, *International Journal of Multiphase Flow* **109** 2018, 164–177, 2018.
- [34] D. Jajcevic, E. Siegmann, C. Radeke, and J. G. Khinast, Large-scale cfd–dem simulations of fluidized granular systems, *Chemical Engineering Science* **98** 2013, 298–310, 2013, ISSN: 0009-2509. DOI: <https://doi.org/10.1016/j.ces.2013.05.014>. [Online]. Available: <http://www.sciencedirect.com/science/article/pii/S000925091300345X>.
- [35] T. Tang, Y. He, T. Tai, and D. Wen, Dem numerical investigation of wet particle flow behaviors in multiple-spout fluidized beds, *Chemical Engineering Science* **172** 2017, 79–99, 2017, ISSN: 0009-2509. DOI: <https://doi.org/10.1016/j.ces.2017.06.025>. [Online]. Available: <http://www.sciencedirect.com/science/article/pii/S0009250917304153>.
- [36] L. Liang, R. Anders, I. Andy, J. Mats, R. Johan, von Corswant Christian, Folestad, and Staffan, Pept study of particle cycle and residence time distributions in a wurster fluid bed, *AIChE Journal* **61**, no. 3 2015, 756–768, 2015. DOI: 10.1002/aic.14692. eprint: <https://aiche.onlinelibrary.wiley.com/doi/pdf/10.1002/aic.14692>. [Online]. Available: <https://aiche.onlinelibrary.wiley.com/doi/abs/10.1002/aic.14692>.
- [37] H. Versteeg and W. Malalasekera, *An Introduction to Computational Fluid Dynamics: The Finite Volume Approach*. Longman Scientific & Technical, 1995, ISBN: 9780582218840. [Online]. Available: <https://books.google.se/books?id=7UynjgEACAAJ>.
- [38] M. Syamlal and D. Gidaspow, Hydrodynamics of fluidization: Prediction of wall to bed heat transfer coefficients, *AIChE Journal* **31**, no. 1 1985, 127–135, 1985. DOI: 10.1002/aic.690310115. eprint: <https://aiche.onlinelibrary.wiley.com/doi/pdf/10.1002/aic.690310115>. [Online]. Available: <https://aiche.onlinelibrary.wiley.com/doi/abs/10.1002/aic.690310115>.

- [39] M. S. van Buijtenen, N. G. Deen, S. Heinrich, S. Antonyuk, and J. A. M. Kuipers, A discrete element study of wet particle particle interaction during granulation in a spout fluidized bed, *The Canadian Journal of Chemical Engineering* **87**, no. 2 2009, 308–317, 2009. DOI: 10.1002/cjce.20144. eprint: <https://onlinelibrary.wiley.com/doi/pdf/10.1002/cjce.20144>. [Online]. Available: <https://onlinelibrary.wiley.com/doi/abs/10.1002/cjce.20144>.
- [40] C. Thornton, S. J. Cummins, and P. W. Cleary, An investigation of the comparative behaviour of alternative contact force models during elastic collisions, *Powder Technology* **210**, no. 3 2011, 189–197, 2011, ISSN: 0032-5910. DOI: <https://doi.org/10.1016/j.powtec.2011.01.013>. [Online]. Available: <http://www.sciencedirect.com/science/article/pii/S0032591011000325>.
- [41] K. L. Johnson, *Contact Mechanics*. Cambridge University Press, 1985. DOI: 10.1017/CB09781139171731.
- [42] R. D. Mindlin, Compliance of elastic bodies in contact, *J. Appl. Mech., ASME* **16** 1949, 259–268, 1949. [Online]. Available: <https://ci.nii.ac.jp/naid/10013415139/en/>.
- [43] J. Ai, J.-F. Chen, J. M. Rotter, and J. Y. Ooi, Assessment of rolling resistance models in discrete element simulations, *Powder Technology* **206**, no. 3 2011, 269–282, 2011, ISSN: 0032-5910. DOI: <https://doi.org/10.1016/j.powtec.2010.09.030>. [Online]. Available: <http://www.sciencedirect.com/science/article/pii/S0032591010005164>.
- [44] D. Gunn, Transfer of heat or mass to particles in fixed and fluidised beds, *International Journal of Heat and Mass Transfer* **21**, no. 4 1978, 467–476, 1978, ISSN: 0017-9310. DOI: [https://doi.org/10.1016/0017-9310\(78\)90080-7](https://doi.org/10.1016/0017-9310(78)90080-7). [Online]. Available: <http://www.sciencedirect.com/science/article/pii/0017931078900807>.
- [45] S. Ergun, Fluid flow through packed columns, *Fluid Flow Through Packed Columns* 1952, 89–94, 1952, cited By 14.
- [46] C. Wen and Y. Yu 1966, 100–111, 1966, cited By 1.
- [47] R. J. Hill, D. L. Koch, and A. J. C. Ladd, The first effects of fluid inertia on flows in ordered and random arrays of spheres, *Journal of Fluid Mechanics* **448** 2001, 213–241, 2001. DOI: 10.1017/S0022112001005948.
- [48] R. Beetstra, M. A. van der Hoef, and J. A. M. Kuipers, Drag force of intermediate reynolds number flow past mono- and bidisperse arrays of spheres, *AIChE Journal* **53**, no. 2 2007, 489–501, 2007. DOI: 10.1002/aic.11065. eprint: <https://onlinelibrary.wiley.com/doi/pdf/10.1002/aic.11065>. [Online]. Available: <https://onlinelibrary.wiley.com/doi/abs/10.1002/aic.11065>.
- [49] C. Romero Luna, I. Avila, L. R. CARROCCI, and G. Arce, A cfd assessment of drag models performance on gas-solid flow hydrodynamics in a fluidized bed Feb. 2015, 5202–5218, Feb. 2015. DOI: 10.5151/chemeng-cobeq2014-0017-27527-160466.
- [50] J. P. V. Doormaal and G. D. Raithby, Enhancements of the simple method for predicting incompressible fluid flows, *Numerical Heat Transfer* **7**, no. 2 1984, 147–163, 1984. DOI: 10.1080/01495728408961817. eprint: <https://doi.org/10.1080/01495728408961817>. [Online]. Available: <https://doi.org/10.1080/01495728408961817>.
- [51] C. RHIE and W. CHOW, Numerical study of the turbulent flow past an airfoil with trailing edge separation, *AIAA Journal* **21**, no. 11 1983, 1525–1532, 1983. DOI: 10.2514/3.8284. eprint: <https://doi.org/10.2514/3.8284>. [Online]. Available: <https://doi.org/10.2514/3.8284>.
- [52] D. Kafui, S. Johnson, C. Thornton, and J. Seville, Parallelization of a lagrangian–eulerian dem/cfd code for application to fluidized beds, *Powder Technology* **207**, no. 1 2011, 270–278, 2011, ISSN: 0032-5910. DOI: <https://doi.org/10.1016/j.powtec.2010.11.008>. [Online]. Available: <http://www.sciencedirect.com/science/article/pii/S0032591010005887>.
- [53] C. A. Radeke, B. J. Glasser, and J. G. Khinast, Large-scale powder mixer simulations using massively parallel gpuarchitectures, *Chemical Engineering Science* **65**, no. 24 2010, 6435–6442, 2010, ISSN: 0009-2509. DOI: <https://doi.org/10.1016/j.ces.2010.09.035>. [Online]. Available: <http://www.sciencedirect.com/science/article/pii/S0009250910005737>.

- [54] C. O’Sullivan and J. D. Bray, Selecting a suitable time step for discrete element simulations that use the central difference time integration scheme, *Engineering Computations* **21**, no. 2/3/4 2004, 278–303, 2004. DOI: 10.1108/02644400410519794.
- [55] J. Lundberg and B. M Halvorsen, A review of some existing drag models describing the interaction between phases in a bubbling fluidized bed, *Proc. Proc. 49th Scand. Conf. Simulation and Modeling* Jan. 2008, Jan. 2008.
- [56] L. Li, J. Remmelgas, B. G. van Wachem, C. von Corswant, M. Johansson, S. Folestad, and A. Rasmuson, Residence time distributions of different size particles in the spray zone of a wurster fluid bed studied using dem-cfd, *Powder Technology* **280** 2015, 124–134, 2015, ISSN: 0032-5910. DOI: <https://doi.org/10.1016/j.powtec.2015.04.031>. [Online]. Available: <http://www.sciencedirect.com/science/article/pii/S0032591015003058>.
- [57] S. Al-Arkawazi, Modeling the heat transfer between fluid-granular medium, *Applied Thermal Engineering* **128** 2018, 696–705, 2018, ISSN: 1359-4311. DOI: <https://doi.org/10.1016/j.applthermaleng.2017.09.064>. [Online]. Available: <http://www.sciencedirect.com/science/article/pii/S1359431117344307>.
- [58] D. Gunn, Transfer of heat or mass to particles in fixed and fluidised beds, *Int. J. Heat Mass Transfer* **21** Apr. 1978, 467–476, Apr. 1978. DOI: 10.1016/0017-9310(78)90080-7.
- [59] R. Kolakaluri, “Direct numerical simulations and analytical modeling of granular filtration”, 2015.
- [60] R. J. Hill, D. L. Koch, and A. J. C. Ladd, Moderate-reynolds-number flows in ordered and random arrays of spheres, *Journal of Fluid Mechanics* **448** 2001, 243–278, 2001. DOI: 10.1017/S0022112001005936.
- [61] T. Mikami, H. Kamiya, and M. Horio, Numerical simulation of cohesive powder behavior in a fluidized bed, *Chemical Engineering Science* **53**, no. 10 1998, 1927–1940, 1998, ISSN: 0009-2509. DOI: [https://doi.org/10.1016/S0009-2509\(97\)00325-4](https://doi.org/10.1016/S0009-2509(97)00325-4). [Online]. Available: <http://www.sciencedirect.com/science/article/pii/S0009250997003254>.
- [62] G. H. Findenegg, J. n. israelachvili: Intermolecular and surface forces (with applications to colloidal and biological systems). academic press, london, orlando, san diego, new york, toronto, montreal, sydney, tokyo 1985. 296 seiten, preis: \$ 65.00. *Berichte der Bunsengesellschaft für physikalische Chemie* **90**, no. 12 1986, 1241–1242, 1986. DOI: 10.1002/bbpc.19860901226. eprint: <https://onlinelibrary.wiley.com/doi/pdf/10.1002/bbpc.19860901226>. [Online]. Available: <https://onlinelibrary.wiley.com/doi/abs/10.1002/bbpc.19860901226>.
- [63] R. B. Bird, Transport phenomena 1960, 1960.
- [64] B. Adam M .J Edmondson, Forces between particles in continuous and discrete liquid media, *Tribology in Particulate technology* 1987, 1987.
- [65] G. Lian, M. J. Adams, and C. Thornton, Elastohydrodynamic collisions of solid spheres, *Journal of Fluid Mechanics* **311** 1996, 141–152, 1996. DOI: 10.1017/S0022112096002534.
- [66] C. Song, D. Liu, J. Ma, and X. Chen, Cfd-dem simulation of flow pattern and particle velocity in a fluidized bed with wet particles, *Powder Technology* **314** 2017, 346–354, 2017, Special Issue on Simulation and Modelling of Particulate Systems, ISSN: 0032-5910. DOI: <https://doi.org/10.1016/j.powtec.2016.10.044>. [Online]. Available: <http://www.sciencedirect.com/science/article/pii/S0032591016307264>.
- [67] T. B. Anderson and R. Jackson, Fluid mechanical description of fluidized beds. equations of motion, *Industrial & Engineering Chemistry Fundamentals* **6**, no. 4 1967, 527–539, 1967. DOI: 10.1021/i160024a007. eprint: <https://doi.org/10.1021/i160024a007>. [Online]. Available: <https://doi.org/10.1021/i160024a007>.
- [68] J. R. Grace, Multiphase flow and fluidization: Continuum and kinetic theory descriptions by d. gidaspow, 1994, 467 + xx pages, academic press, san diego, ca, isbn 0-12-282470-9. price: Us \$69.50, *The Canadian Journal of Chemical Engineering* **73**, no. 5 1995, 784–784, 1995. DOI:

- 10.1002/cjce.5450730523. eprint: <https://onlinelibrary.wiley.com/doi/pdf/10.1002/cjce.5450730523>. [Online]. Available: <https://onlinelibrary.wiley.com/doi/abs/10.1002/cjce.5450730523>.
- [69] B. Crüger, V. Salikov, S. Heinrich, S. Antonyuk, V. Sutkar, N. Deen, and J. Kuipers, Coefficient of restitution for particles impacting on wet surfaces: An improved experimental approach, *Particuology* **25** 2016, 1–9, 2016, ISSN: 1674-2001. DOI: <https://doi.org/10.1016/j.partic.2015.04.002>. [Online]. Available: <http://www.sciencedirect.com/science/article/pii/S1674200115001157>.
- [70] T. Müller and K. Huang, Influence of the liquid film thickness on the coefficient of restitution for wet particles, *Phys. Rev. E* **93** 4 2016, 042904, 4 2016. DOI: 10.1103/PhysRevE.93.042904. [Online]. Available: <https://link.aps.org/doi/10.1103/PhysRevE.93.042904>.
- [71] T. Kawaguchi, M. Sakamoto, T. Tanaka, and Y. Tsuji, Quasi-three-dimensional numerical simulation of spouted beds in cylinder, *Powder Technology* **109**, no. 1 2000, 3–12, 2000, ISSN: 0032-5910. DOI: [https://doi.org/10.1016/S0032-5910\(99\)00222-3](https://doi.org/10.1016/S0032-5910(99)00222-3). [Online]. Available: <http://www.sciencedirect.com/science/article/pii/S0032591099002223>.
- [72] C. Thornton and C. Randall, Applications of theoretical contact mechanics to solid particle system simulation, *Micromechanics of Granular Materials, Satake and Jenkins (eds)* **20** Jan. 1988, 133–142, Jan. 1988. DOI: 10.1016/B978-0-444-70523-5.50023-0.
- [73] C. M. Hrenya and J. L. Sinclair, Effects of particle-phase turbulence in gas-solid flows, *AIChE Journal* **43**, no. 4 1997, 853–869, 1997. DOI: 10.1002/aic.690430402. eprint: <https://aiche.onlinelibrary.wiley.com/doi/pdf/10.1002/aic.690430402>. [Online]. Available: <https://aiche.onlinelibrary.wiley.com/doi/abs/10.1002/aic.690430402>.
- [74] M. R. Maxey and J. J. Riley, Equation of motion for a small rigid sphere in a nonuniform flow, *The Physics of Fluids* **26**, no. 4 1983, 883–889, 1983. DOI: 10.1063/1.864230. eprint: <https://aip.scitation.org/doi/pdf/10.1063/1.86423>. [Online]. Available: <https://aip.scitation.org/doi/abs/10.1063/1.86423>.
- [75] C. T. Crowe, J. D. Schwarzkopf, and M. S. and Yutaka Tsuji, *Multiphase Flows with Droplets and Particles, The Science of Microfabrication*. CRC Press, 2011.
- [76] E. Teunou and D. Poncelet, Batch and continuous fluid bed coating – review and state of the art, *Journal of Food Engineering* **53**, no. 4 2002, 325–340, 2002, ISSN: 0260-8774. DOI: [https://doi.org/10.1016/S0260-8774\(01\)00173-X](https://doi.org/10.1016/S0260-8774(01)00173-X). [Online]. Available: <http://www.sciencedirect.com/science/article/pii/S026087740100173X>.
- [77] J. R. Grace, Multiphase flow and fluidization: Continuum and kinetic theory descriptions, *The Canadian Journal of Chemical Engineering* **73**, no. 5 1994, 784–784, 1994. DOI: 10.1002/cjce.5450730523.